# Chapter 34 – LESSONS LEARNED FROM THE NUMERICAL INVESTIGATIONS ON THE VFE-2 CONFIGURATION

by

**Willy Fritz[1] and Russell M. Cummings[2]**

The Second International Vortex Flow Experiment provided a variety of experimental data for a 65° delta wing with sharp and blunt/rounded leading edges. Flow measurements including forces and moments, surface pressures, Pressure Sensitive Paint measurements, and off-surface flow variables from Particle Image Velocimetry were made available for comparisons with computational simulations. A number of test cases were chosen for simulation by seven numerical groups, and a summary of their results is presented here. The ability of computational fluid dynamics to predict such flow features as the dual primary vortex system found on the blunt leading edge configuration and a shock/vortex interaction for the sharp leading edge are assessed. While computational simulation has made great strides in recent years, there are still areas where further improvement can be made, including in turbulence modeling, transition modeling, and the ability to accurately compute unsteady flows.

## 34.1 NOMENCLATURE

| | | |
|---|---|---|
| $A$ | = | wing aspect ratio, $\equiv b^2 / S$ |
| $a$ | = | speed of sound |
| $b$ | = | wing span |
| $C_p$ | = | pressure coefficient, $\equiv (p - p_\infty) / q_\infty$ |
| $c_f$ | = | local skin friction coefficient, $\equiv \tau / q_\infty$ |
| $c_{mac}$ | = | mean aerodynamic chord, $= 2c_r / 3$ (also $c_{bar}$) |
| $c_r$ | = | root chord (also $c$) |
| $d$ | = | sting diameter |
| $M$ | = | Mach number, $\equiv V / a$ |
| $p$ | = | pressure |
| $q$ | = | dynamic pressure, $\equiv \rho V^2 / 2 = \gamma p M^2 / 2$ |
| $Re$ | = | Reynolds number based on mean aerodynamic chord, $\equiv V_\infty c_{mac} / \upsilon$ |
| $r_{le}$ | = | leading edge radius |
| $S$ | = | wing planform area |
| $t$ | = | wing maximum thickness |
| $V$ | = | velocity |
| $x$ | = | longitudinal dimension ($x = 0$ at apex of wing) |

[1] Senior Development Engineer, Aerodynamics & Methods.

[2] Professor of Aeronautics, Department of Aeronautics.

| | | |
|---|---|---|
| $x_v$ | = | position of vortex origin |
| $\alpha$ | = | angle of attack, deg |
| $\gamma$ | = | ratio of specific heats |
| $\eta$ | = | normalized local half span of the wing ≡ *2y/b* |
| $\Lambda$ | = | wing leading edge sweep angle, deg |
| $\lambda$ | = | wing taper ratio, $\equiv c_t / c_r$ |
| $\rho$ | = | density |
| $\tau$ | = | shear stress |
| $\upsilon$ | = | kinematic viscosity |
| $\infty$ | = | free stream condition |

| | | |
|---|---|---|
| DLR | = | German Aerospace Center / Germany |
| EADS | = | European Aeronautic Defence and Space Company / Germany |
| KTH | = | Royal Institute of Technology / Sweden |
| NASA | = | National Aeronautics and Space Administration / United States |
| NLR | = | National Aerospace Laboratory / Netherlands |
| UG | = | University of Glasgow / UK |
| USAFA | = | US Air Force Academy / United States |

## 34.2 INTRODUCTION

The Second International Vortex Flow Experiment (VFE-2) is the outgrowth of a very successful First International Vortex Flow Experiment (VFE-1) program that took place from 1984 through 1986 [34-1]. VFE-1 was an experimental program that was undertaken to provide experimental data for the rapidly improving computational fluid dynamics (CFD) capabilities of the time. Euler calculations for delta wings in the early 1980s had progressed to such a state that improved experiments would be necessary to provide CFD simulations with important data for validation and verification of predictions. The VFE-1 configuration (see Figure 34-1) was a 65° sweep leading-edge clipped delta wing with a sharp leading edge and a fuselage. The experiments recorded surface pressures at three chord wise locations, as well as force measurements and flow field visualization. The results of VFE-1 were summarized in [34-2], and later reviews were made of the state-of-the-art in Euler code simulations in [34-3], [34-4]. Even for sharp leading edge delta wings with fixed primary separation, the Euler codes were not well suited to calculate the pressure distributions properly since the secondary vortex separation was not simulated by the inviscid equations.

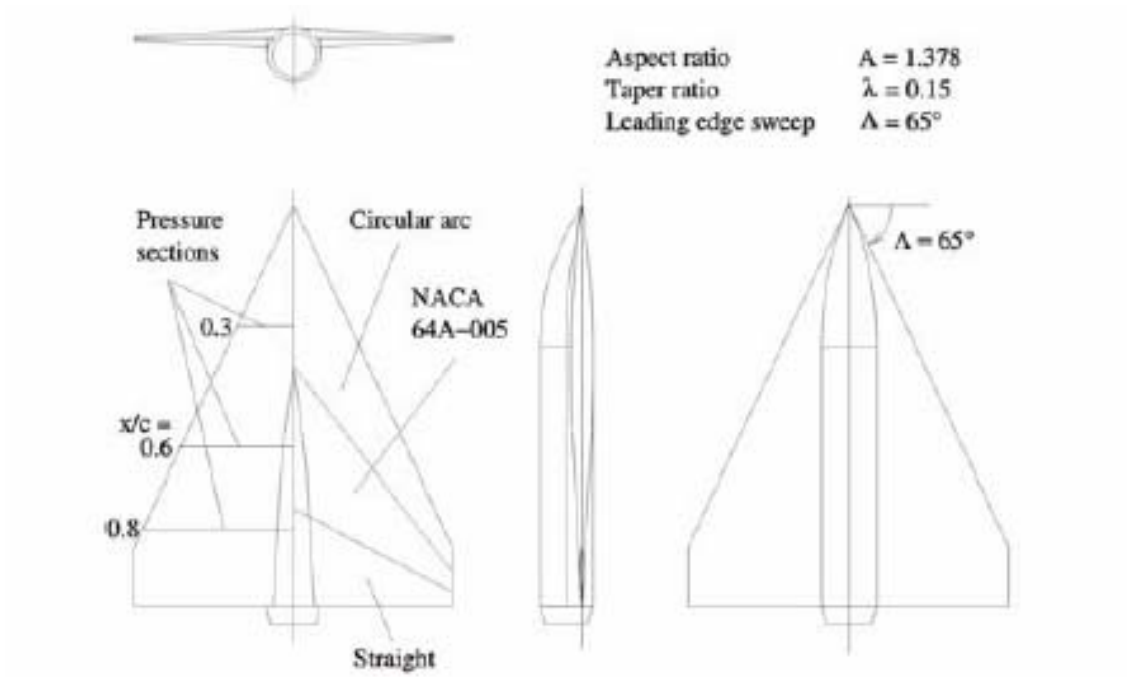


**Figure 34-1: Configuration of the First International Vortex Flow Experiment (VFE-1); Ref. [34-1].**

Since the mid 1980s it has become commonplace to simulate delta wing flows using the Navier-Stokes equations. Initially Reynolds-Averaged Navier-Stokes (RANS) simulations were performed, first with algebraic turbulence models, and later with 1- and 2-equation turbulence models [34-5]. In recent years, hybrid turbulence models have also been applied to the flow around delta wings with good success [34-6]. RANS simulations were able to predict secondary (and even tertiary) vortex separation, but issues with turbulence models often led to poor prediction of the surface pressures, especially the location and strength of the secondary vortices. This led to a need for improved experimental data for delta wings, and improved computational simulation methods, especially improvements in turbulence models.

In order to validate the results of Navier-Stokes calculations, new and more detailed experimental data are required, which led to a Second International Vortex Flow Experiment (VFE-2, see Ref. [34-7] and Chapter 17). The configuration for VFE-2 was chosen to create distinct flow regimes, including:

1) Attached flow without vortex formation, $0^\circ \le \alpha \le 4^\circ$
2) Separated vortical flow without vortex breakdown, $4^\circ \le \alpha \le 20^\circ$
3) Separated vortical flow with vortex breakdown, $20^\circ \le \alpha \le 40^\circ$
4) Separated deadwater flow, $40^\circ \le \alpha \le 90^\circ$

A delta wing with a leading edge sweep of 65° was chosen for the experiments with a flat plate inner portion in combination with interchangeable leading edges. Four leading edge configurations were chosen: a sharp leading edge, and three rounded leading edges of varying radii. The configuration, shown in Figure 34-2, had been initially tested at NASA Langley Research Center (Ref. [34-9] and Chapter 18), and additional experiments have been conducted at a variety of locations, including DLR in Germany (see Chapter 19), ONERA in France

(Chapter 20), TU Munich (Chapter 21), The University of Glasgow (Chapter 22), and Tübitak in Turkey (Chapter 23). The objectives for the VFE-2 experiments include (Ref. [34-8] and Chapter 17):

1) Investigations of laminar/turbulent transition on delta wings.
2) Detailed pressure distribution measurements, especially in the region of the onset of flow separation for configurations with rounded leading edges.
3) Boundary layer measurements including distributions of the components of velocity, vorticity, turbulent energy, and eddy viscosity.
4) Determination of the wall shear stress and detection of the secondary and tertiary separation lines.
5) Flow field measurements in the primary and secondary vortices including the distributions of the components of velocity, vorticity, turbulent energy, and eddy viscosity.
6) Investigations on the vortex breakdown flow field for delta wings with sharp and rounded leading edges including the surface pressure fluctuations caused by the spiral mode of vortex breakdown.

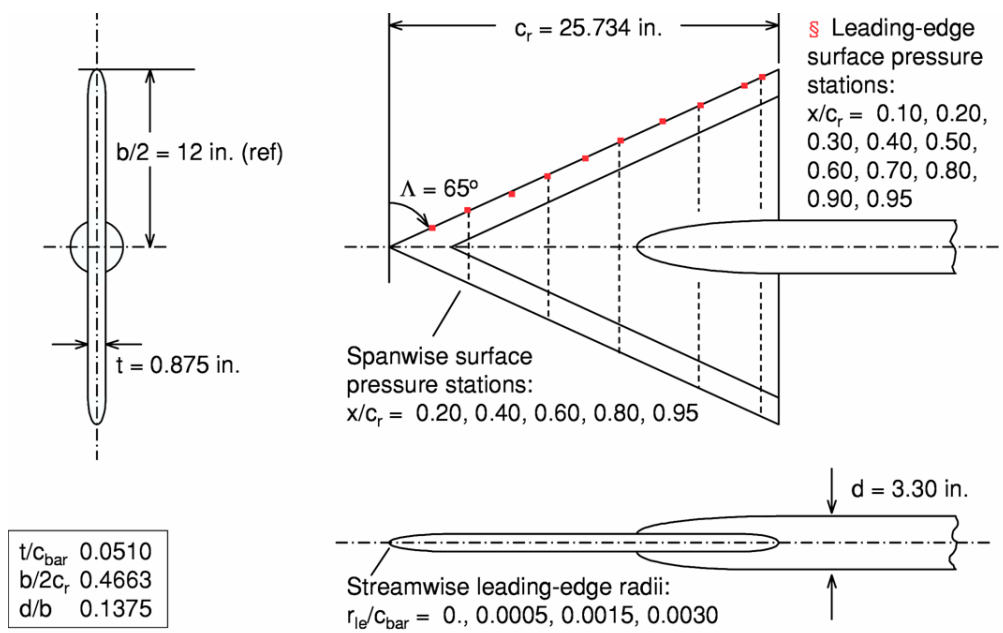


**Figure 34-2: Configuration of the Second International Vortex Flow Experiment (VFE-2); Ref. [34-9].**

Limited previous numerical simulations have been conducted to match the NASA Langley Research Center VFE-2 experiments. Londenberg performed simulations for a sharp leading edge transonic case in 1994 (in conjunction with the original wind tunnel tests) (Ref. [34-10]). Also, Chiba and Obayashi showed simulations of the dual primary vortex system for the rounded leading edge configuration [34-11]. The interesting topology of the dual primary vortex system led to the majority of numerical simulations for VFE-2. VFE-2 was formed as a Task Group (AVT-113) under the NATO Research and Technology Organization's Applied Vehicle Technology Panel. Numerical simulations were performed by participants from seven organizations in six countries (Germany, The Netherlands, Sweden, Turkey, United Kingdom, and United States). The majority of this paper serves as a summary for the numerical predictions that were presented in a special session at the AIAA 46th Aerospace Sciences Meeting, including in Refs. [34-12] through [34-17].

## 34.3 GOALS FOR THE VFE-2 NUMERICAL SOLUTIONS

Since the quantity of data and tested flow conditions for VFE-2 was quite large ([34-18] and Chapter 24), the CFD simulations were chosen to concentrate on about thirty specific flow/geometry combinations (see Appendix 34-1). Of these, a specific subset was chosen as representative of the various simulations, including:

1) Onset of vortical flow:
   a) Sharp leading edge: Separated flow
   b) Medium radius leading edge: Partly attached, partly separated flow

2) Separated flow without vortex breakdown:
   a) Sharp leading edge
   b) Medium radius leading edge

3) Separated flow with vortex breakdown:
   a) Sharp leading edge
   b) Medium radius leading edge

4) Transonic flow with vortex breakdown

This led to comparisons for the cases shown in Table 34-1 that will be presented in this review.

**Table 34-1: CFD Cases Chosen for Summary Comparison**

| Case No. | Leading Edge* | Mach No., $M_\infty$ | Angle of Attack, α (deg) | Reynolds Number, Re |
|---|---|---|---|---|
| 4.5 | MRLE | 0.4 | 13 | $3 \times 10^6$ |
| 5 | MRLE | 0.4 | 13 | $6 \times 10^6$ |
| 14 | MRLE | 0.4 | 18 | $6 \times 10^6$ |
| 15 | SLE | 0.4 | 18 | $6 \times 10^6$ |
| 24 | SLE | 0.4 | 23 | $6 \times 10^6$ |
| 27 | SLE | 0.85 | 23 | $6 \times 10^6$ |

*MRLE: Medium Radius Leading Edge; SLE: Sharp Leading Edge

## 34.4 ROUNDED LEADING EDGE FLOW TOPOLOGY

The rounded leading edge delta wing was the primary configuration chosen for study because the early wind tunnel experiments at NASA Langley Research Center had shown unusual flow features. Specifically, two primary, co-rotating, vortices were seen which were dramatically different than the vortex system found for delta wings with sharp leading edges. Sharp leading edge delta wings have primary vortices that roll up from the shear layer that separates along the sharp edge from the apex of the delta wing (see Figure 34-3). These vortices produce secondary vortices on the upper surface that form due to boundary layer separation from the

outboard flow induced by the primary vortices. Because the separation location is fixed, the flow is only mildly sensitive to Reynolds number, but flow properties also vary with angle of attack and Mach number. Rounded (or blunt) leading edge delta wings have quite different flow fields, however. Specifically, because the separation location is not fixed, the flow exhibits a displaced vortex origin that varies strongly with angle of attack, Mach number, Reynolds number, and leading-edge radius. In addition, a dual primary vortex structure develops for these flows (see Figure 34-4).

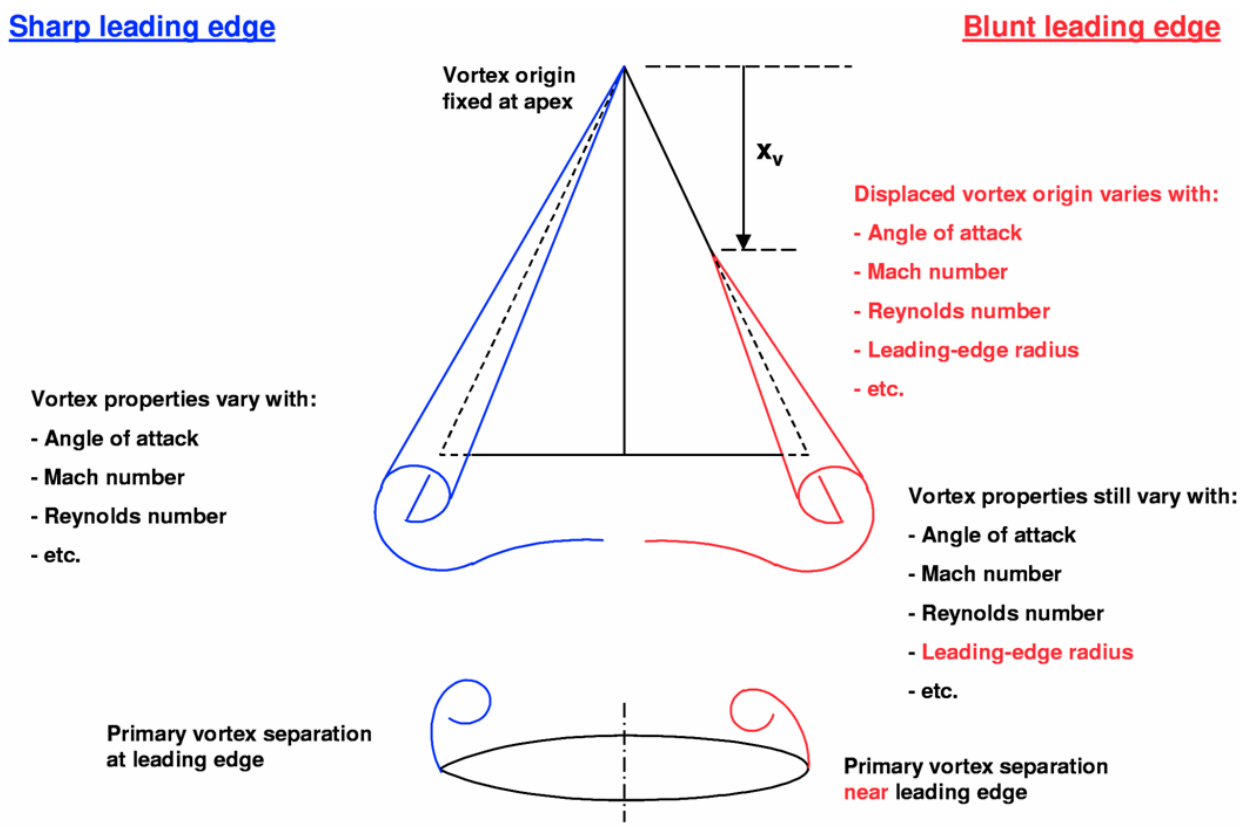


**Figure 34-3: Comparison of Vortical Flow Features for Sharp and Rounded Leading Edge Delta Wings; Ref. [34-9] and Chapter 18.**

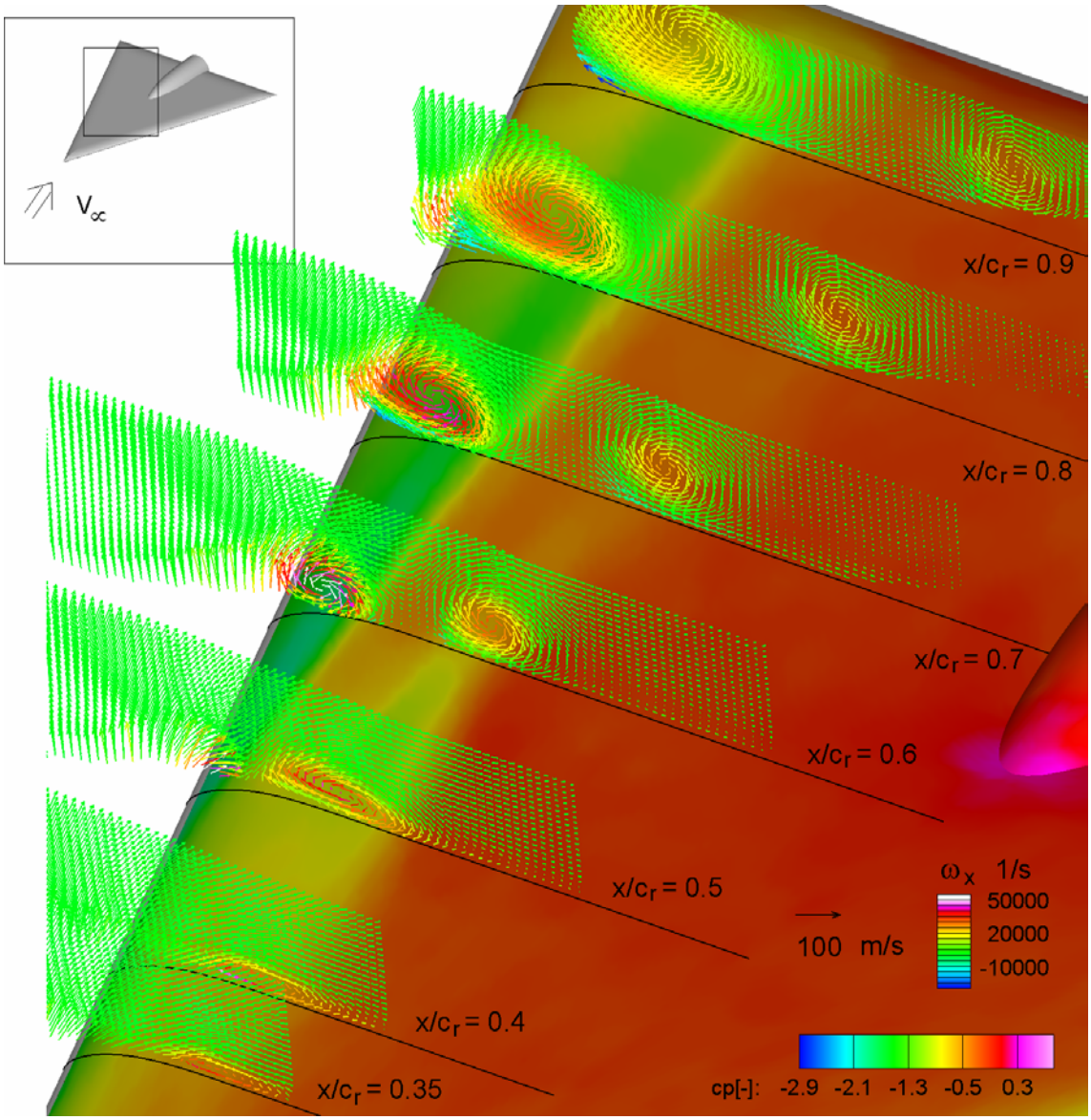


**Figure 34-4: Dual Primary Vortex System for MRLE Delta Wing with PIV and PSP, M = 0.4, Re = 3 x $10^6$, α = 13°; Ref. [34-19] and Chapter 19.**

## 34.5 COMPUTER CODES AND TURBULENCE MODELS

One of the important aspects of the VFE-2 working group was to determine the abilities and capabilities of modern CFD Navier-Stokes codes and turbulence models to properly simulate the flows found in the wind tunnel experiments. A group of researchers from seven organizations in six countries simulated various combinations of the test cases, and results for those simulations will be summarized and discussed here. Table 34-2 shows the organizations, codes, and turbulence models used in the following simulations. Refs. [34-12] through [34-17] and Chapters 25 through 32 should be referred to for details about the particular codes, grids, and turbulence models.

**Table 34-2: Organization, Codes, and Turbulence Models for CFD Simulations**

| Organization | Grid Type | Grid Size | Code | Turbulence Models |
|---|---|---|---|---|
| EADS | Block Structured | ~10 x $10^6$ | FLOWer | Wilcox k-ω |
| KTH | Unstructured, adapted | up to 7 x $10^6$ | EDGE | EARSM + Hellsten k-ω |
| NLR | Block Structured | ~4 x $10^6$ | ENFLO | TNT k-ω + vorticity correction |
| TAI | Block Structured | ~2 x $10^6$ | TAI-xFlowg | SA |
| UG | Block Structured | ~7 x $10^6$ | PM3D | TNT k-ω + vorticity correction |
| DLR | Unstructured | ~16 x $10^6$ | Tau | SA, Wilcox k-ω |
| USAFA | Unstructured | ~26 x $10^6$ | Cobalt | SA and SA-DES |

## 34.6 RESULTS AND DISCUSSIONS

Various solutions for the six cases described in Table 34-1 will be presented and compared in this section. The goal is not to show comparisons of every solution, rather to show a representative set of comparisons so that appropriate conclusions can be drawn about the state of the art in simulating these complex flow fields.

### 34.6.1 Case 4.5: MRLE, M = 0.40, α = 13°, Re = 3 x $10^6$

This case was a cryptic test case for a very long time. As Figure 34-5 shows, there are the footprints of two vortices in the surface pressure distribution. Besides the classical main leading edge vortex, which begins at a certain distance from the apex of the wing due to the rounded leading edges, there is also a second primary vortex more inboard. The stream traces show that both vortices have the same sense of rotation. The inner vortex is formed by a flow separation in the front region of the wing, which rolls up into a longitudinal vortex. (By their torsion the 3-D volume ribbons also indicate the local vorticity).

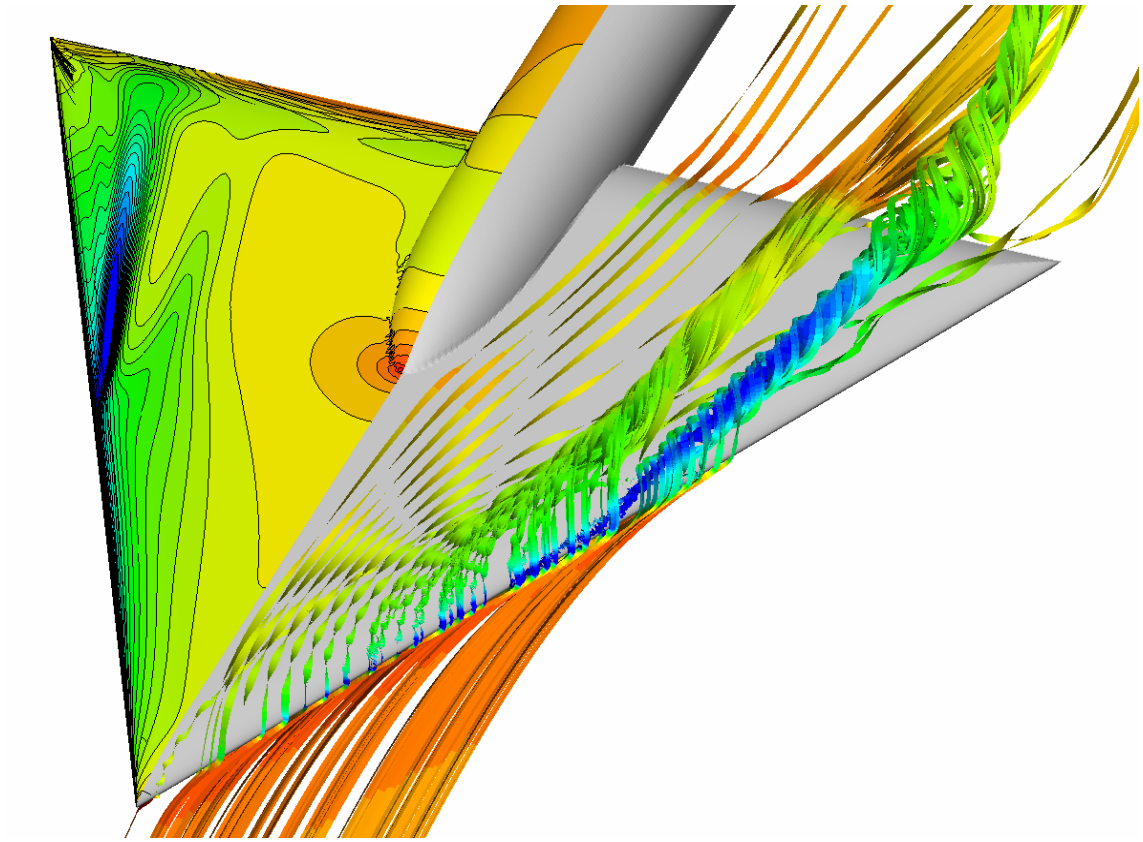

**Figure 34-5: Flow Features for Case 4.5: MRLE, M = 0.40, α = 13°, Re = 3 x $10^6$ (Surface Pressure Contours and Streamtraces by 3-D Volume Ribbons, Colored by Local $C_p$ Values).**

A detailed discussion of this complicated flow field is given in the individual chapters of the contributors, and in the Refs. [34-12]-[34-17], [34-19]. In order for the numerical solutions to provide quantitatively correct results, it is important that the onset of the main primary separation is fairly well predicted. A more up- or downstream position of this separation point will lead to large differences in the surface pressure distribution, in addition to other aspects of the flow field. A second challenge for the numerical methods is the separation in the forward region of the wing, which leads to the inner vortex. The strength and the position of the inner vortex affect the second suction peak in the surface pressure distribution. The strength of this inner vortex (and the effect on the surface pressure distribution) depends very much on the position of the leading edge separation. As soon as this leading edge vortex has reached certain strength, the inner vortex is no longer fed, since it is separated from the shear layer coming from the leading edge. From this longitudinal position (and downstream), the inner vortex weakens and finally dissipates. If the predicted formation point for the inner vortex is too much upstream, leading edge separation produces a very weak inner vortex which dissipates very early. All these details are, of course, strongly affected by the grid resolution, the quality of the turbulence model, and also the transition location (due to the round leading edge).

Figure 34-6 shows a comparison of different numerical surface pressure contours with those of the PSP experiment of DLR (Ref. [34-19] and Chapter 19). The dashed horizontal line indicates the onset of the main primary separation in the experiment. The prediction of this vortex onset is the main difference between the different numerical solutions. The EADS-solutions has this separation point slightly behind, but very close to,

the experimental separation point. The other solutions show a slightly more upstream position (DLR, TAI, and USAFA) or a considerable more upstream position (KTH). Except for the TAI-solution. All other solutions show the footprint of the inner vortex. Possibly the TAI-grid with 2 million grid points is not fine enough to resolve this flow feature. As can also be seen, none of the solutions exactly match the experimental surface pressure pattern.

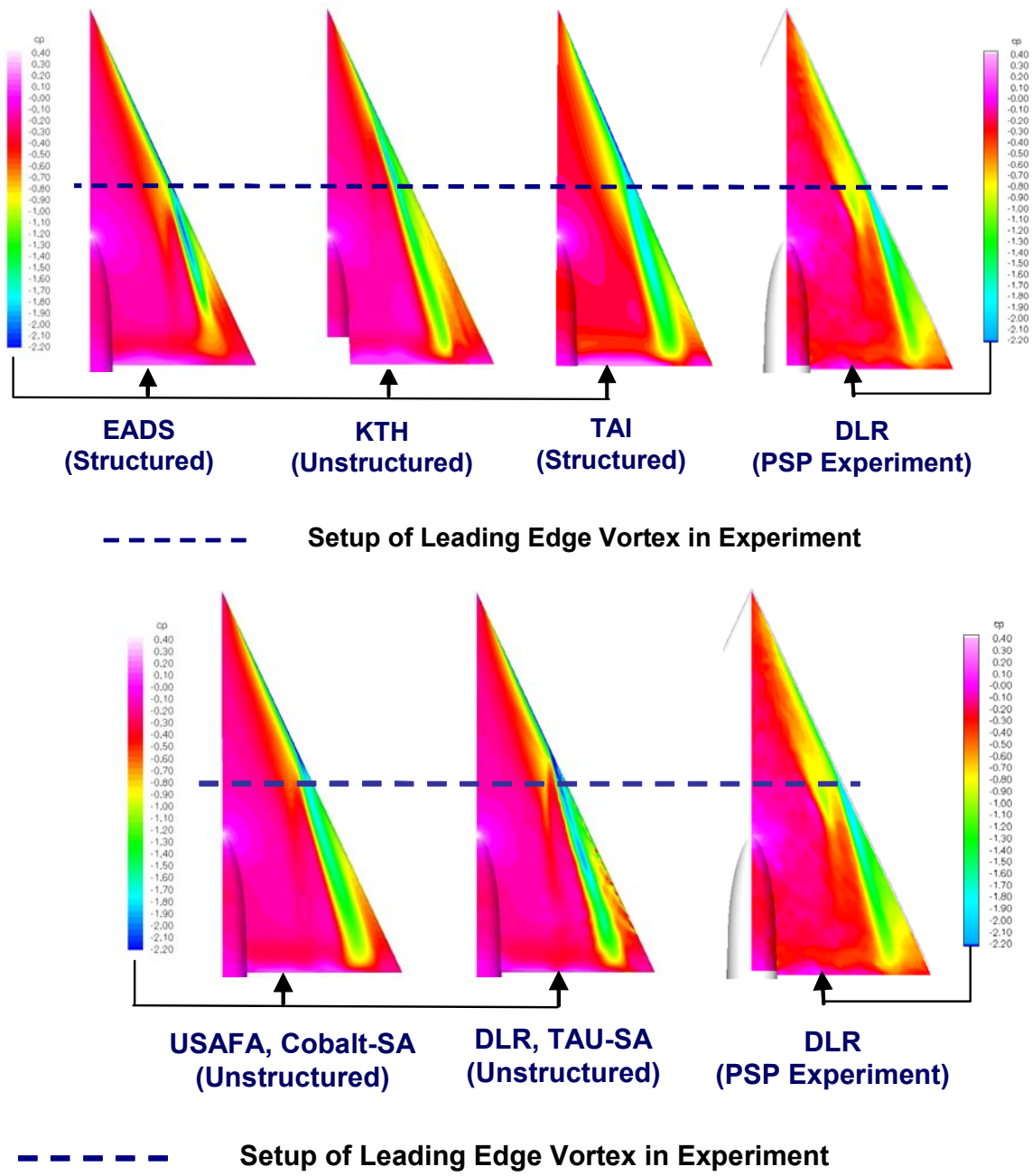


**Figure 34-6: Surface Pressure Maps and Onset of Leading-Edge Vortex for Case 4.5: MRLE, M = 0.40, α = 13°, Re = 3 x $10^6$.**

A more detailed comparison of the surface pressure distribution is given in Figure 34-7. At the first cross section shown ($x/c_r = 0.2$), where no leading edge separation occurs, all the numerical pressure distributions are identical and agree with the experimental data. There is a similar situation at $x/c_r = 0.4$; four of the five numerical pressure distributions still show no leading edge separation and thus are identical and agree very well with the experimental data. The KTH solution already shows the effect of a primary vortex and differs from the other solutions. The experimental pressure distribution in this section already shows an effect of the beginning of the inner vortex. This effect can slightly be seen in the KTH solution.

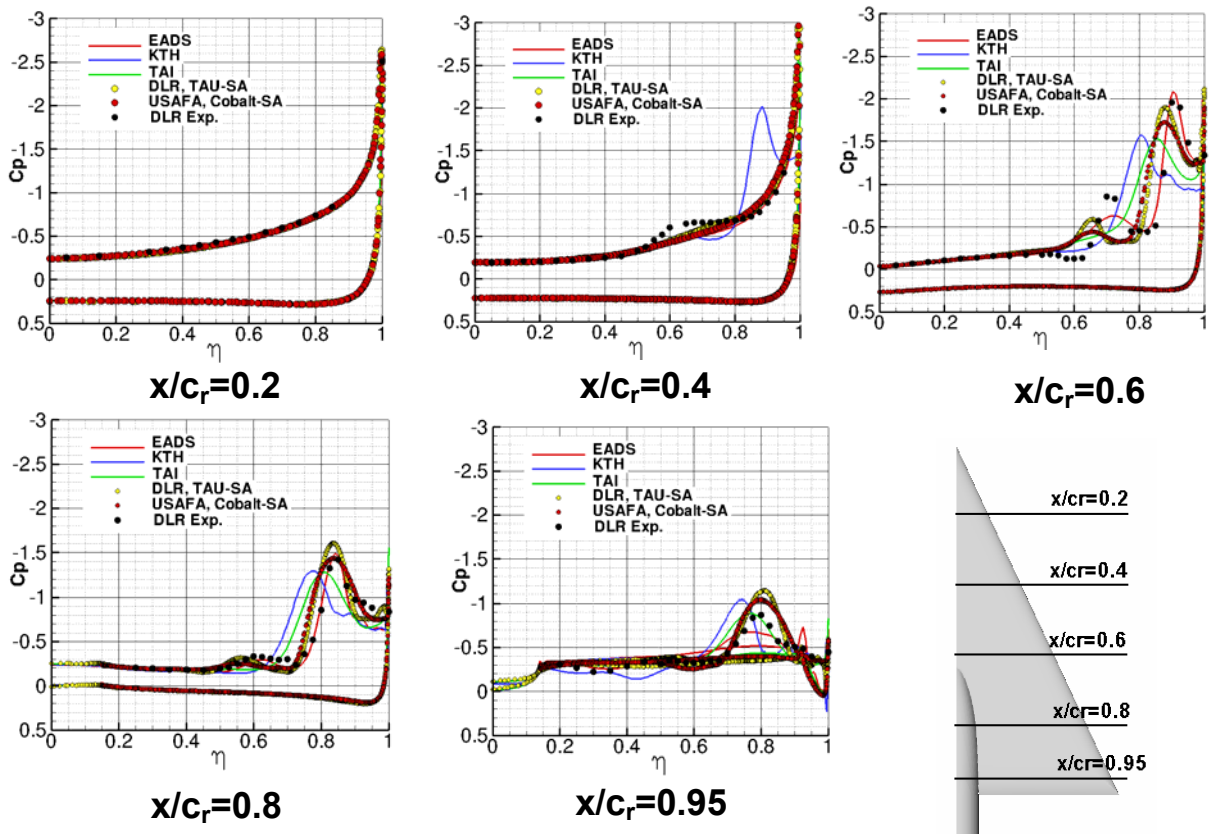


**Figure 34-7: Comparison of Surface Pressures and Experimental Data (Ref. [34-19]) for Case 4.5: MRLE, M = 0.40, α = 13°, Re = 3 x $10^6$.**

At $x/c_r = 0.6$, all solutions and the experimental data clearly show a primary vortex. There are differences in the position and the magnitude of the leeward suction peak due to this primary vortex. These differences can be related to the onset of the primary leading edge separation. The more upstream this separation occurs, the more inboard the suction peak moves due to the primary vortex at this cross section. The experimental data also show very clearly the effect of the second, inner vortex. As already mentioned above, the foot print of this second vortex is not present in the TAI solution. In the KTH solution, this inner vortex is due to the early leading edge separation which is too weak at this cross section. The other three solutions show the effect of this inner vortex. The EADS solution shows this second peak at the correct span wise position. The DLR and USAFA solutions show that the outer primary vortex is already more inboard when compared with the experiment, and the inner suction peak is consequently also more inboard. But in all of these three solutions the inner vortex is too weak when compared to the experiment.

In the cross section $x/_{cr}$ = 0.8 the various results are very similar. The more upstream the leading edge separation occurs, the more inboard the primary vortex is positioned (in the DLR and USAFA solution this can be detected at the position of the inboard pressure gradient). The footprint of the inner vortex has become very weak and those solutions which showed the inner vortex in the cross section $x/c_r$ = 0.6 also show the decrease of this vortex.

At the last cross section, $x/c_r$ = 0.95, the experimental pressure distribution shows a weak primary vortex. This cross section is situated in the region of high surface curvature where the geometry changes from the flat plate to the sharp leading edge. This leads to a significant deceleration of the axial flow. Additionally, all other upstream effects have accumulated in this section. Therefore, the prediction of the flow characteristics in this section is very difficult. This can be seen in the numerical pressure distributions, which scatter from under prediction to over prediction of the suction peak.

Figure 34-8 shows a comparison of the numerical prediction of the skin friction magnitude for this test case. The skin friction distributions are consistent with the surface pressure distributions shown in Figure 34-7. They show more clearly the position and the compactness of the main primary vortex, as well as the inner vortex. The maximum values at the peak of the main primary vortex are very similar. This indicates that the grid resolution in the boundary region is very similar in the different grids.

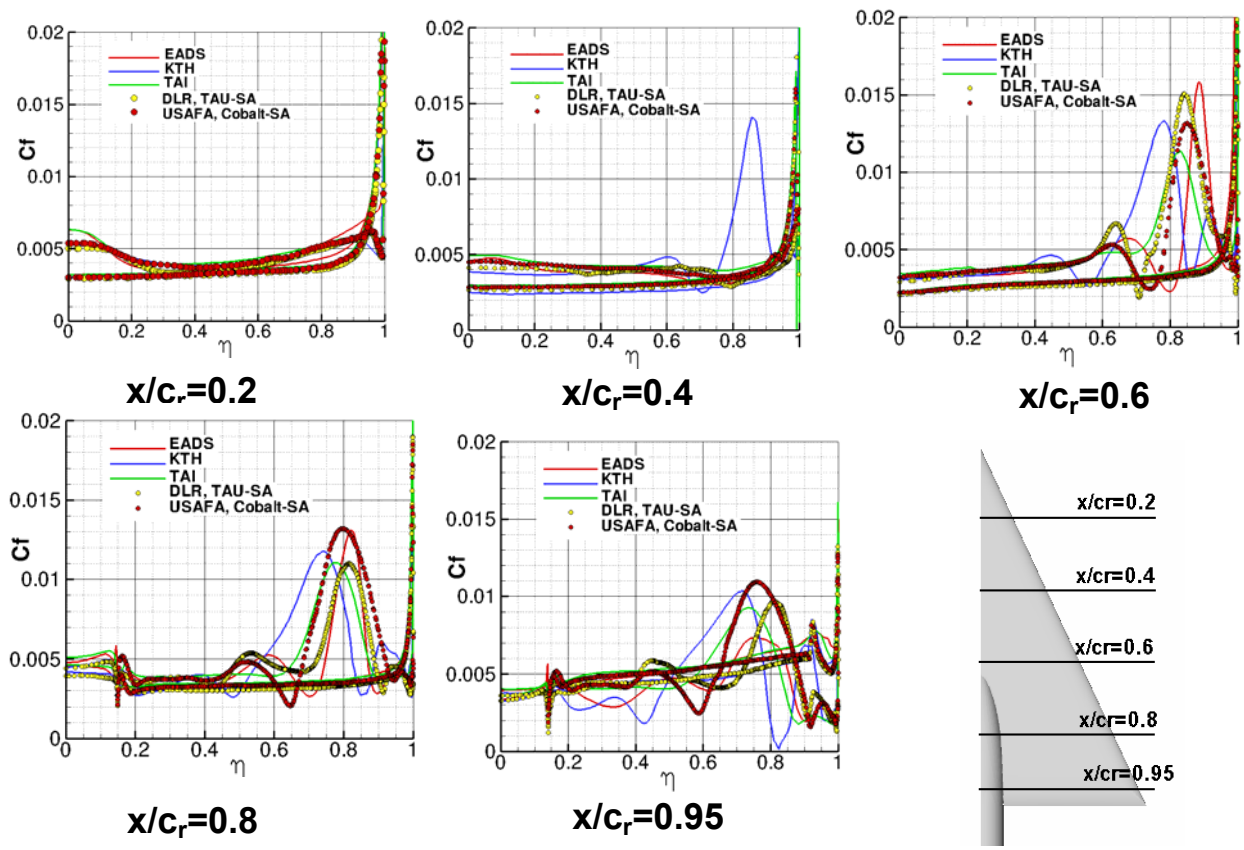


**Figure 34-8: Comparison of Computed Surface Skin Friction Data for Case 4.5: MRLE, M = 0.40, α = 13°, Re = 3 x $10^6$.**

The different surface grids which have been used for this test case are given in Figure 34-9. From these surface grids it can be concluded that the TAI grid is possibly not fine enough for a resolution of the inner vortex. Because of the isotropic surface triangulation, the unstructured grids also have high grid density in the axial direction. The structured grids are both conical grids.

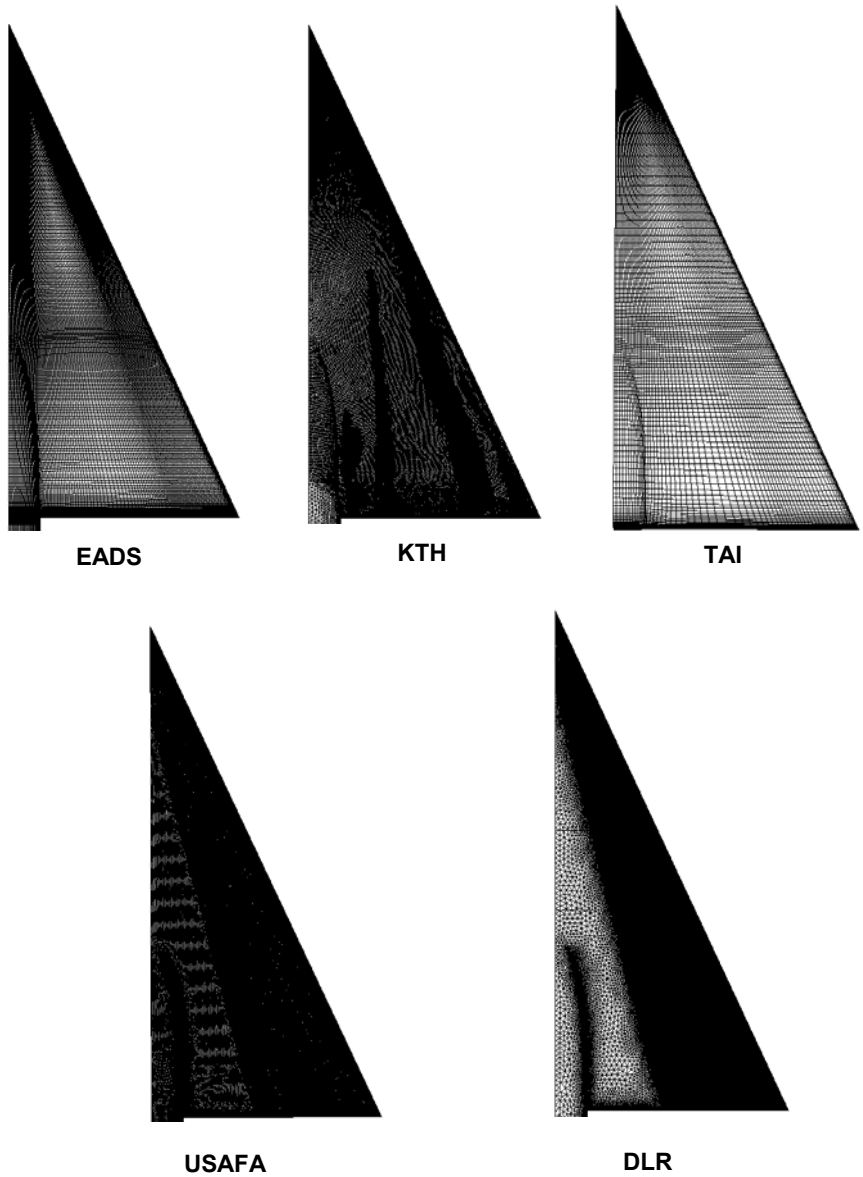


**Figure 34-9: Surface Grid Density Comparison for Various Predictions.**

### 34.6.2 Case 5: MRLE, M = 0.40, α = 13°, Re = 6 x $10^6$

This test case is very similar to Case 4.5 above, but in the experiments two very important differences have been observed. Due to the higher Reynolds number, the leading edge separation is delayed to a more downstream

position. Also due to the higher Reynolds number, the inner vortex is now much weaker when compared with the test case above. The LPTP experimental data from NASA (Ref. [34-9]) are used for comparison with the numerical predictions.

The surface pressure contours of three different typical solutions are presented in Figure 34-10. The horizontal dashed lines mark the onset of the leading edge separation in the different numerical solutions. In the experiment, the onset of the leading edge vortex is somewhere upstream of the cross section $x/c_r = 0.6$. There are very clear differences in the prediction of this leading edge separation. In the EADS solution it occurs more downstream (slightly behind $x/c_r = 0.6$), in the KTH-solution the separation is too much upstream (close to $x/c_r = 0.2$) and in the TAI-solution separation is at $x/c_r = 0.5$. Footprints of the inner vortex are weakly present in the KTH solution and very weakly present in the EADS solution.

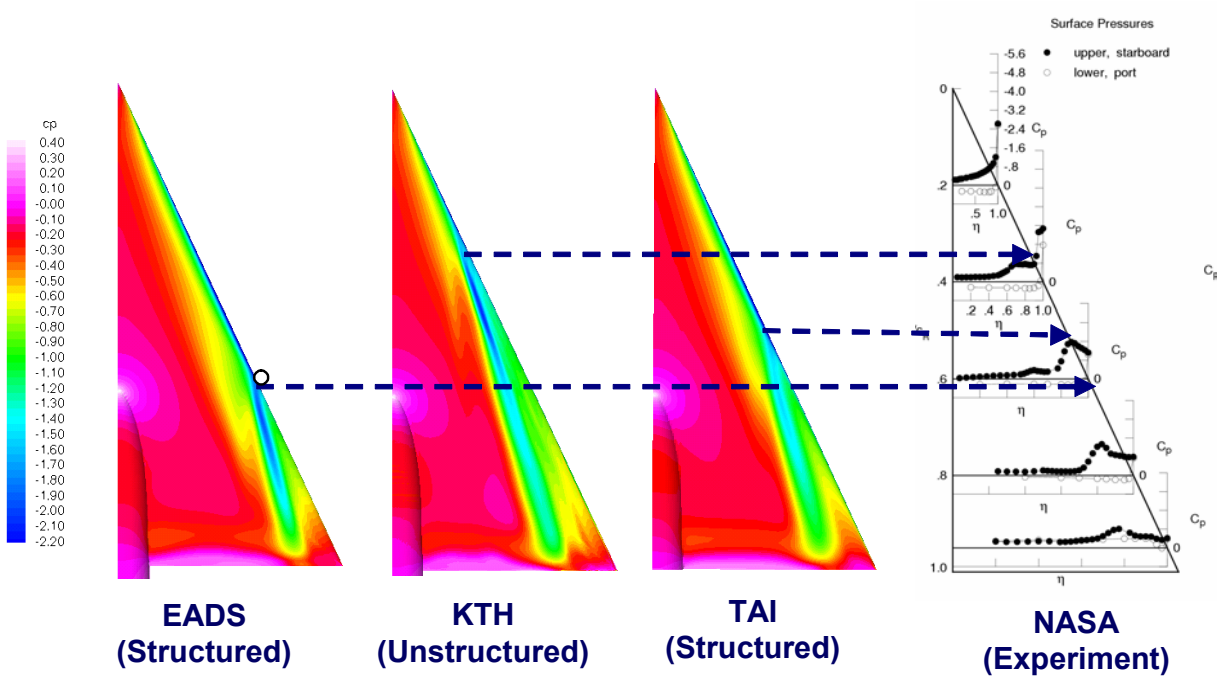


**Figure 34-10: Surface Pressure Maps and Onset of Leading-Edge Vortex for Case 5: MRLE, M = 0.40, α = 13°, Re = 6 x $10^6$.**

Figure 34-11 shows the comparison of the surface pressure distributions for this test case. In the experimental pressure distribution there is only a considerable effect of the inner separation at the cross section $x/c_r = 0.4$, and at $x/c_r = 0.6$ only the effect of a very weak inner vortex can be observed. So for this test case the inner vortex plays only a minor role. The three solutions can be characterized as follows:

- Too early leading edge separation (KTH);
- Too late leading edge separation (EADS); and
- Leading edge separation very close to the experiment (TAI).

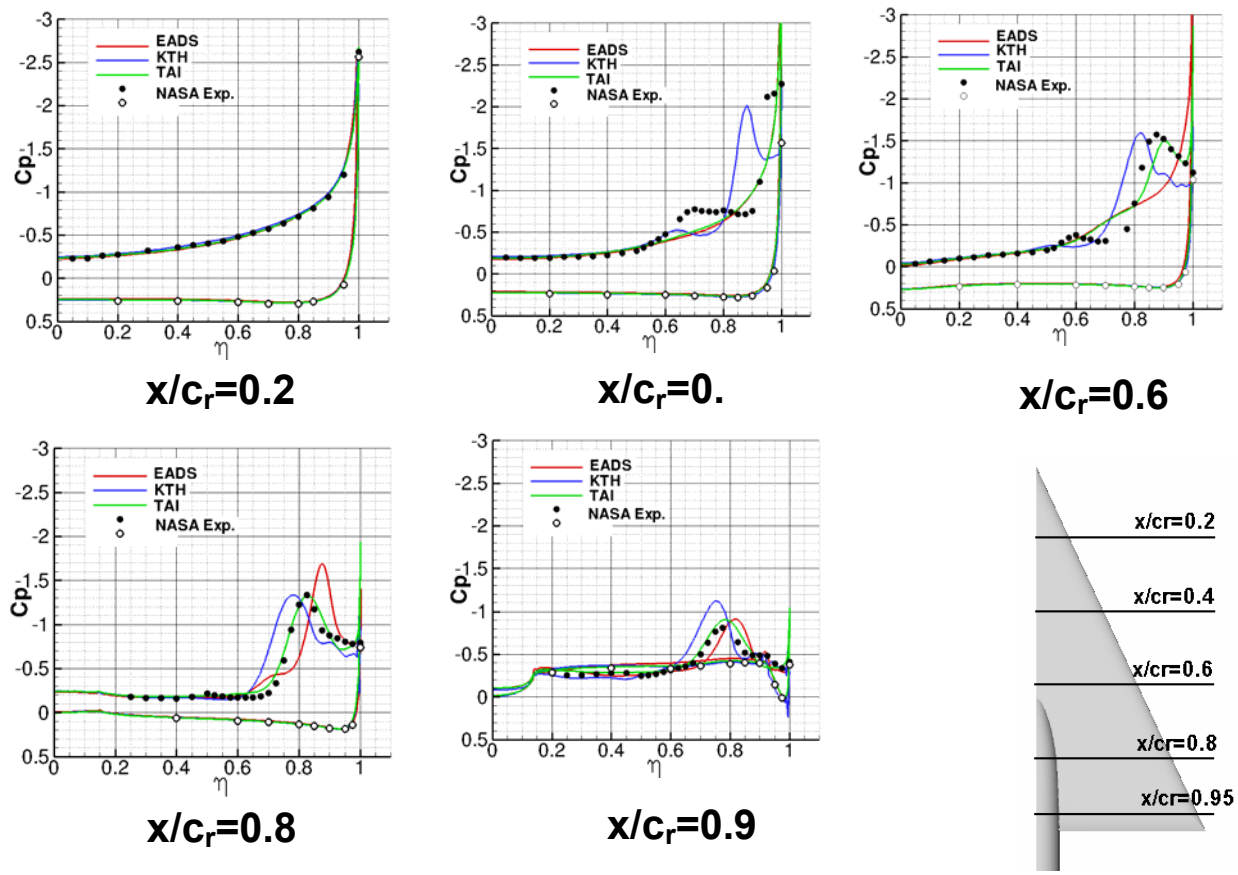


**Figure 34-11: Comparison of Surface Pressures and Experimental Data (Ref. [34-9]) for Case 5: MRLE, M = 0.40, α = 13°, Re = 6 x $10^6$.**

The different surface pressure distributions are consequences of these effects. The more upstream leading edge separation (KTH) leads to a more inboard position of the leeward suction peak. A more delayed separation (EADS) gives a more inboard position. The TAI solution with the leading edge separation very close to the experimental value shows the correct position of the suction peak and matches the experimental data quite well.

There are surely several effects or sensitivities which may influence the onset of this leading edge separation. One effect may be the unknown position of boundary layer transition. (All numerical simulations have been done in fully turbulent mode). In order to asses the effect of transition, a calculation with prescribed transition was performed at EADS. The result is presented in Figure 34-12.

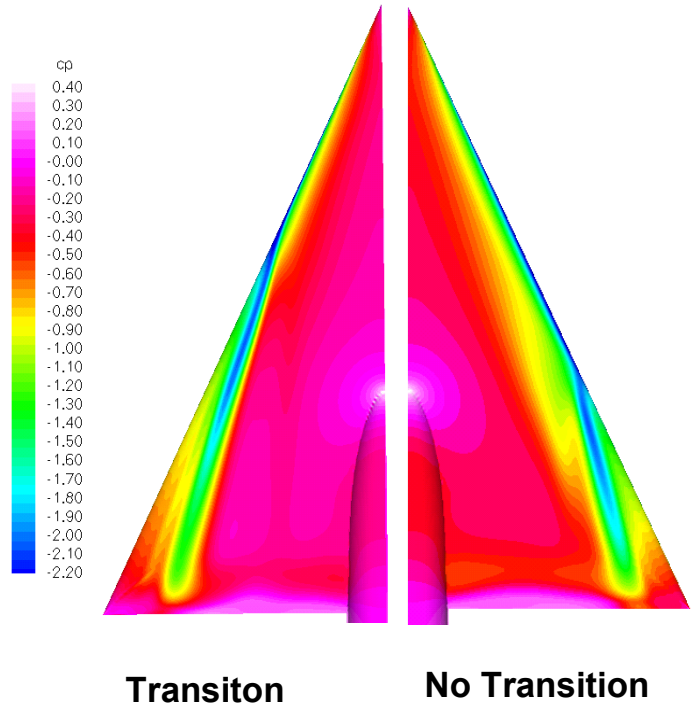


**Figure 34-12: Impact of Transition on Surface Flow for Case 5 (EADS-Solution, see Chapter 25): MRLE, M = 0.40, α = 13°, Re = 6 x $10^6$.**

The transition was specified along a conical line close to the wing leading edge on the upper side of the wing. The distance of this conical section from the leading edge was $\Delta y = 0.006 * b_{local}$. During the calculation the effect of transition is realized by forcing zero production of turbulence within the laminar region. As Figure 34-12 demonstrates, there is a considerable effect on the solution. Up to now it has not been quite clear whether this is a real physical effect, or whether the turbulence model produces too much eddy viscosity around the leading edge, which must be corrected. But in any case this calculation shows that the numerical solution is very sensitive to small variations in the eddy viscosity distribution.

An assessment of the effect of the Reynolds number on the leading edge separation is given in Figure 34-13. From the experiments [34-9] it is known that increasing Reynolds number delays the primary separation location. This effect is not uniform in the different solutions. The EADS solution probably shows a too strong delay, the KTH solution shows no clear effect, and the TAI solution shows a reasonable effect of increasing Reynolds number.

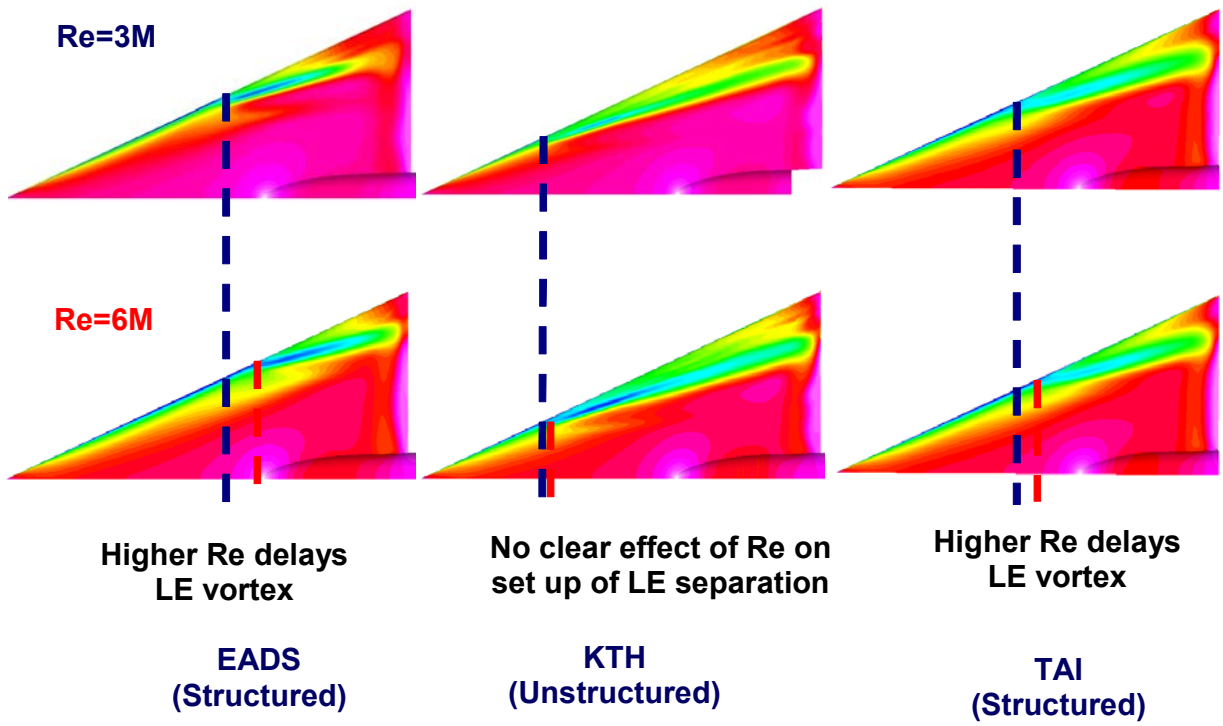


**Figure 34-13: Effect of Reynolds Number on Surface Flows for Case 5: MRLE, M = 0.40, α = 13°, Re = 6 x $10^6$.**

### 34.6.3 Case 14: MRLE, M = 0.40, α = 18°, Re = 6 x $10^6$

The next test case is again the round leading edge geometry, but at a higher angle of attack. The leading edge separation now moves close to the wing apex and the inner vortex has no considerable effect. A fully developed primary vortex without vortex break down should be expected for this case. The vortical flow structure is shown in Figure 34-14, as shown by the EADS solution.

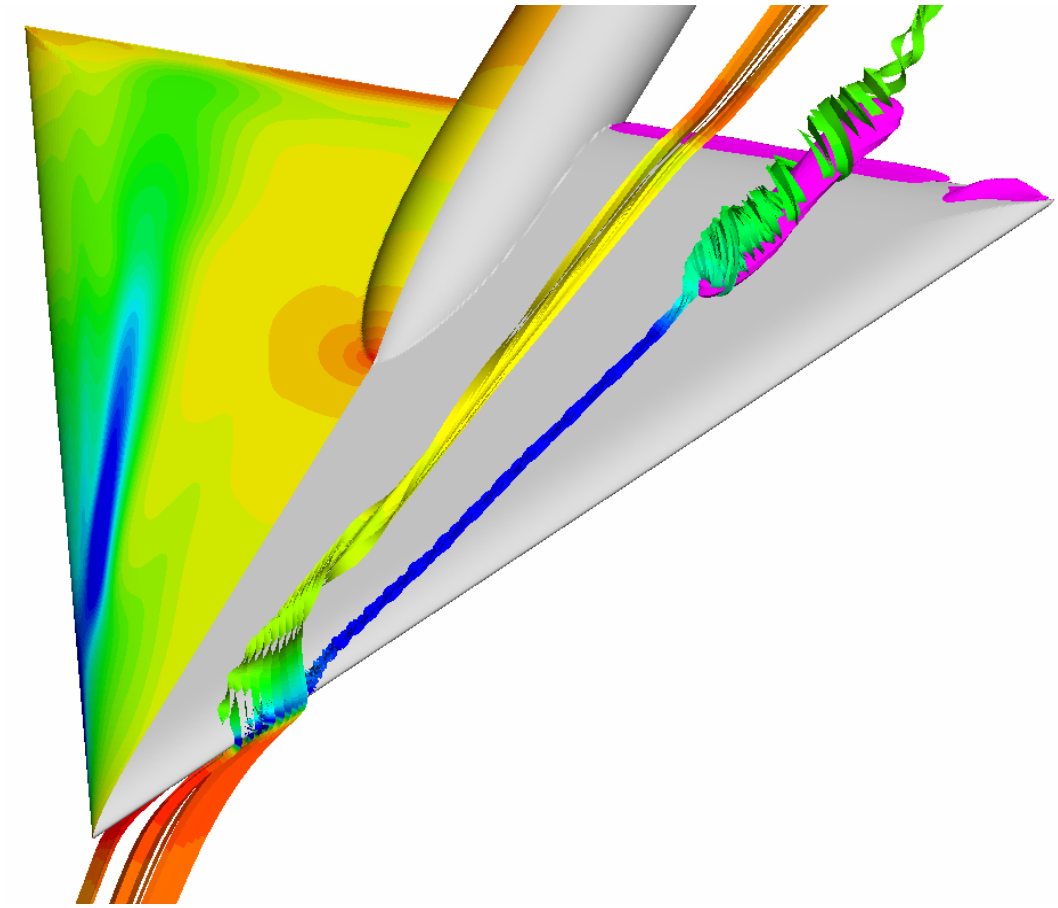

**Figure 34-14: Flow Features for Case 14: MRLE, M = 0.40, α = 18°, Re = 6 x $10^6$.**

In Figure 34-14 the vortical flow structure is visualized again by 3-D volume ribbons. There is a separation at the apex region of the wing which rolls up into a small inner vortex. But this inner vortex only has a small impact on the pressure distribution in the apex region. The leading edge separation now begins very close to the wing apex. The core of the leading edge vortex remains very compact until $x/c_r = 0.8$. At this position the core forms a small bubble until to the rear end of the wing where the core becomes compact again. The pink colored bubble in the figure is an iso-surface of zero axial velocity. Inside the bubble the axial velocity is negative and outside it is positive. Negative axial velocity in the vortex core is a criterion for vortex breakdown, which means that the calculation shows a very weak vortex breakdown. In general for a 65° swept delta wing, vortex breakdown is expected at α = 21°, but the geometry has a highly curved trailing edge region, which induces an additional increase in pressure. This may lead to an earlier vortex breakdown.

Figure 34-15 shows the surface pressure contours for different numerical solutions. The differences in the onset of the leading edge separation are now much smaller and the pressure contours look more similar as in the previous cases. Three solutions (EADS, KTH, DLR) indicate the above mentioned vortex breakdown at the rear end of the wing. In the experimental pressure distributions (NASA LTPT experiments [34-9]) there is a rather compact suction peak up to $x/c_r = 0.8$. At $x/c_r = 0.95$, there is still a vortical flow structure, but the suction peak is smeared out. This may indicate a very weak vortex breakdown at the rear end of the wing (due to the high curvature of the trailing edge).

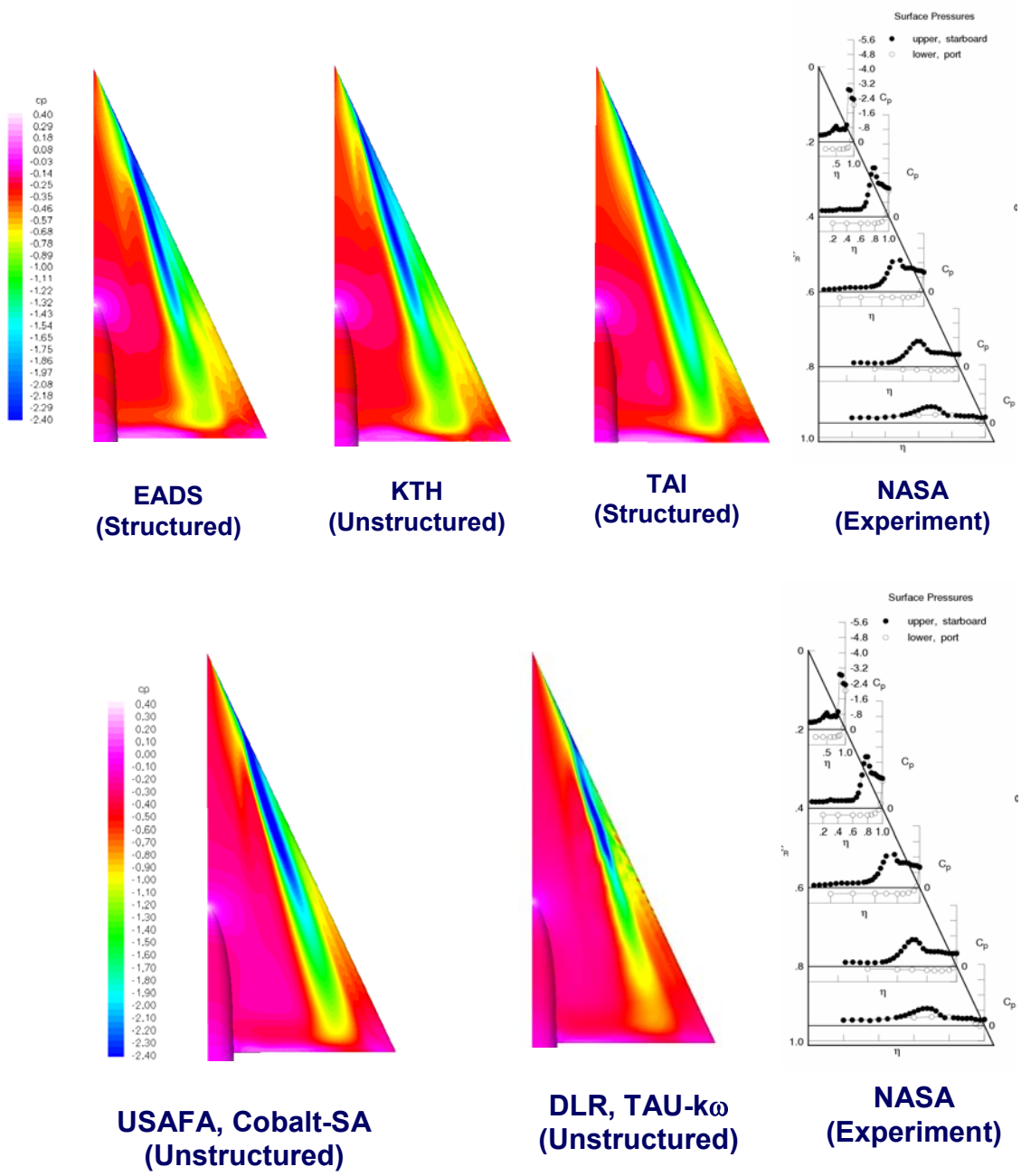


**Figure 34-15: Surface Pressure Maps for Case 14: MRLE, M = 0.40, α = 18°, Re = 6 x $10^6$.**

The surface pressure distributions now agree much better compared to the previous cases (Figure 34-16). Essential differences are at $x/c_r = 0.2$. The KTH solution already clearly shows a primary vortex, but slightly more inboard compared to the experiment. All other solutions do not yet show a primary vortex. This indicates that the KTH solution has the leading edge separation a little bit too early (but very close to the experiment) and that the other solutions have the leading edge separation later when compared with the experiment.

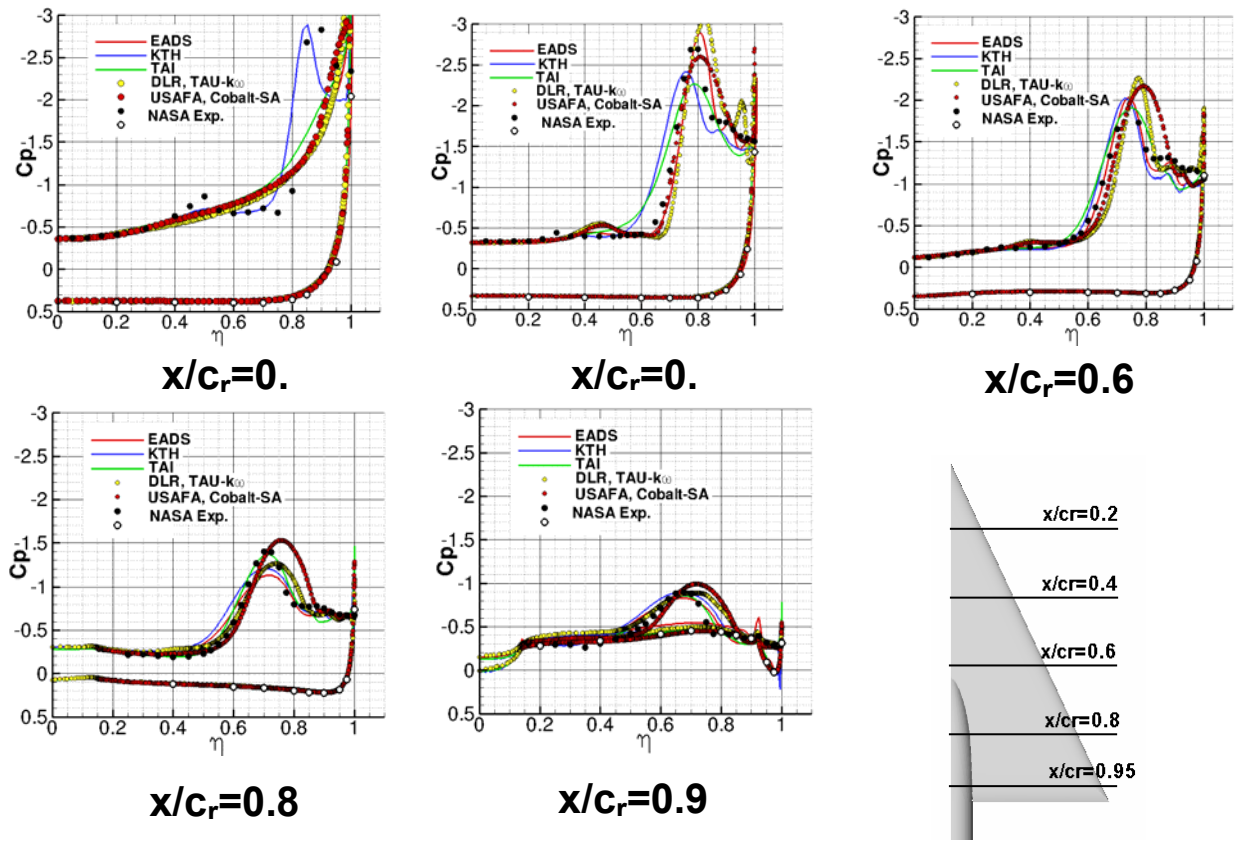


**Figure 34-16: Comparison of Surface Pressures and Experimental Data (Ref. [34-9]) for Case 14: MRLE, M = 0.40, α = 18°, Re = 6 x $10^6$.**

At $x/c_r$ = 0.4 and $x/c_r$ = 0.6 all solutions show the correct flow features. There is a dominating primary vortex and the effect of a secondary vortex (between the leading edge and suction peak). Differences between the different solutions occur mainly in over- or under-prediction of the effects of the secondary vortex and in over- or under-prediction of the main suction peak. These may be effects of the different turbulence models and of the different grid resolutions. At $x/c_r$ = 0.8 the EADS, DLR, and KTH solutions are under-predicting the main suction peak and smearing it out. The reason, therefore, may be the above mentioned spread of the vortex core. At the cross section $x/c_r$ = 0.95 the EADS solution with its weak vortex breakdown matches quite well to the experimental data. This indicates that the above mentioned weak vortex breakdown due to the high curvature of the rear end of the wing is also present in the experiment.

### 34.6.4 Case 15: SLE, M = 0.40, α = 18°, Re = 6 x $10^6$

In this test case the leading edge separation is fixed by the sharp leading edge and the primary vortex formation begins at the wing apex. A well developed primary vortex without vortex breakdown should be expected for this test case. In Figure 34-17 three different solutions for this test case are presented. The solutions all look very similar and all again indicate vortex breakdown over the rear end of the wing (see above section for details).

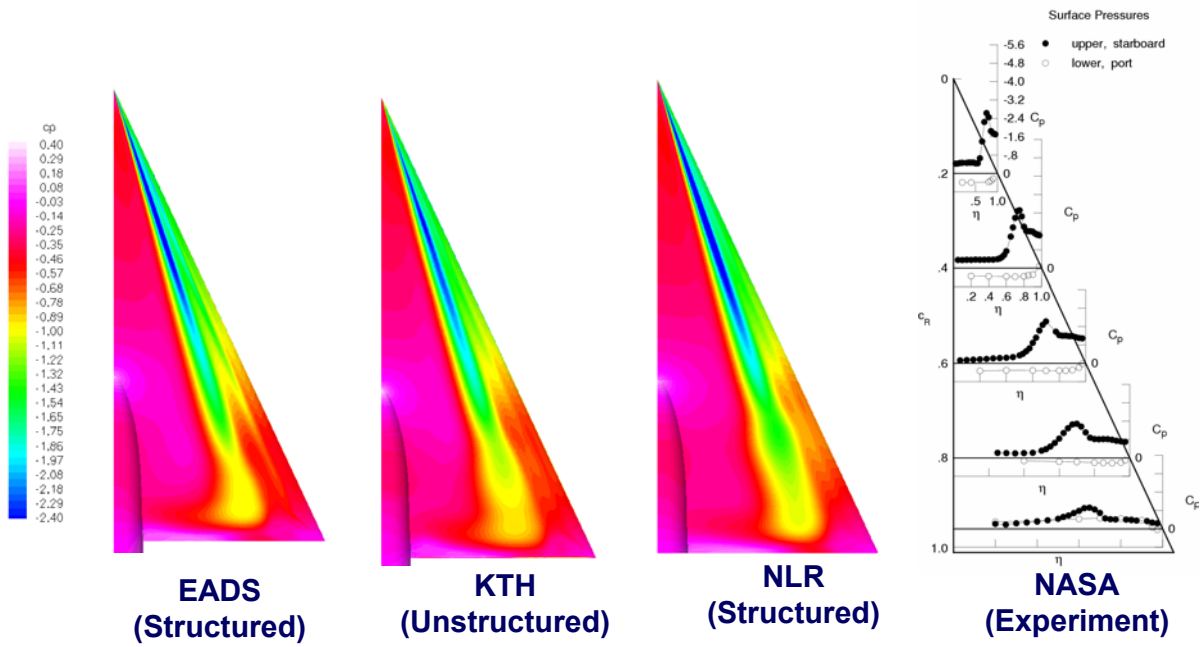


**Figure 34-17: Surface Pressure Maps for Case 15: SLE, M = 0.40, α = 18°, Re = 6 x $10^6$.**

The agreement of the surface pressure distributions up to the cross section $x/c_r = 0.6$ is very good, as shown in Figure 34-18. Differences between the predictions and experiment mainly occur in the level of the maximum suction peak and in the region of the secondary vortex; this is commonly related to the turbulence model. In the cross section $x/c_r = 0.8$, all solutions indicate a less compact suction peak. This can again be related to the spreading of the vortex core in the calculations. In the last cross section the experiment shows a rather compact suction peak (unlike in the previous case), whereas in all calculations the suction peak is smeared out.

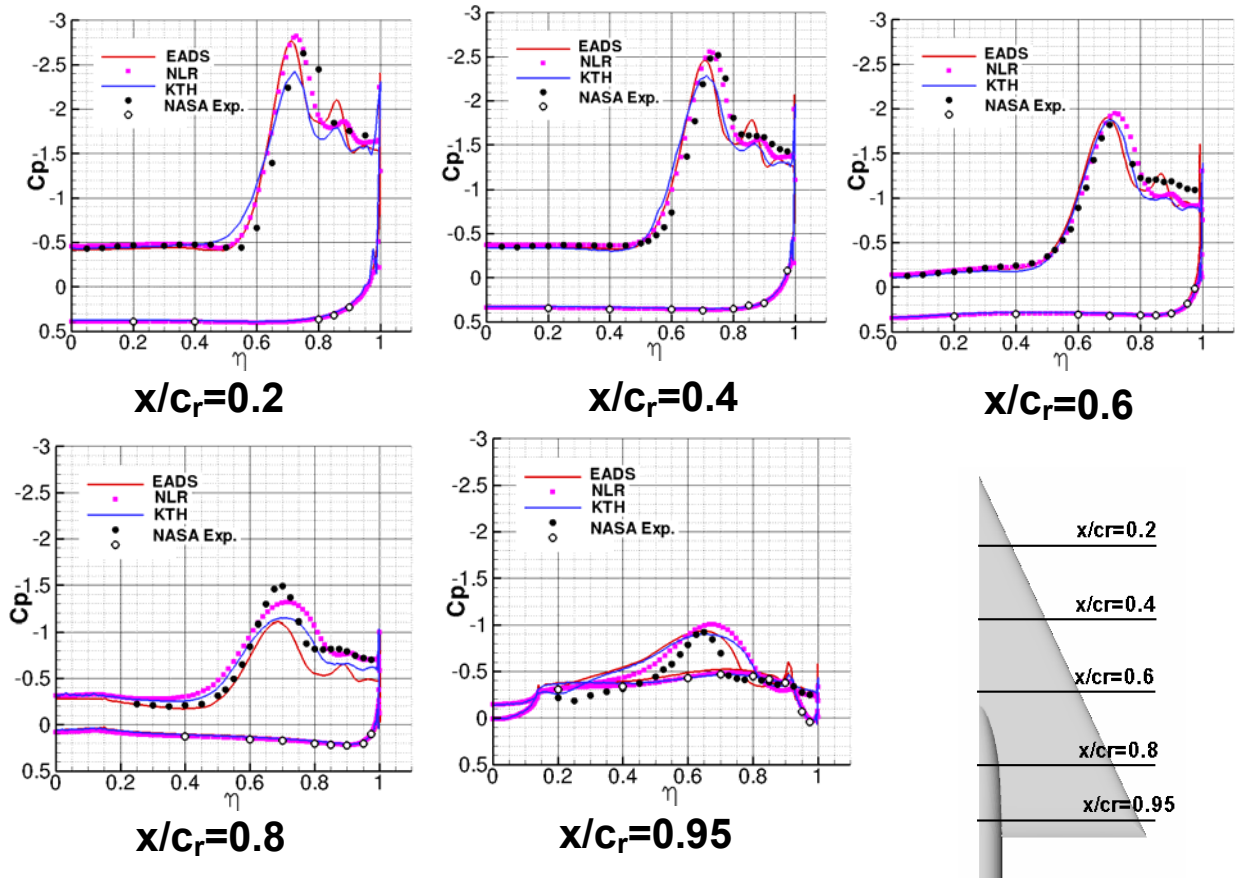


**Figure 34-18: Comparison of Surface Pressures and Experimental Data (Ref. [34-9]) for Case 15: SLE, M = 0.40, α = 18°, Re = 6 x $10^6$.**

### 34.6.5 Case 24: SLE, M = 0.40, α = 23°, Re = 6 x $10^6$

This is again a case where the onset of the leading edge separation is fixed by the sharp leading edge and begins at the wing apex. Unlike Case 15, vortex breakdown is also present in the experiment. Figure 34-19 shows the surface pressure map and the vortical flow structure for this test case using the EADS solution as an example. The 3-D volume ribbons along the vortex core are again colored according to the local $C_p$ values. There is a very compact vortex core up to about $x/c_r$ = 0.6. Then the vortex widens and sidesteps the region with negative axial velocity (which is again indicated by the pink bubble in the figure). This region with negative axial velocity has a small radius but the axial extension is rather large. The widening of the vortex core results in a reduced rotation of the vortex, and by this the leeward suction peak in the surface pressure distribution is cut back, as can be seen in the surface pressure contours on the left hand side of Figure 34-19. From the rather long bubble with negative axial velocities in Figure 34-19 it can be assumed that the axial velocities in the vortex core are under-predicted in the different numerical methods. As different numerical methods with different turbulence models and different grids have been used for the calculations, the results seem to not be an issue of grid resolution. Also, different turbulence models do not affect the prediction a great deal. In fact it seems that the turbulence models still have a difficulty with respect to vortical flow.

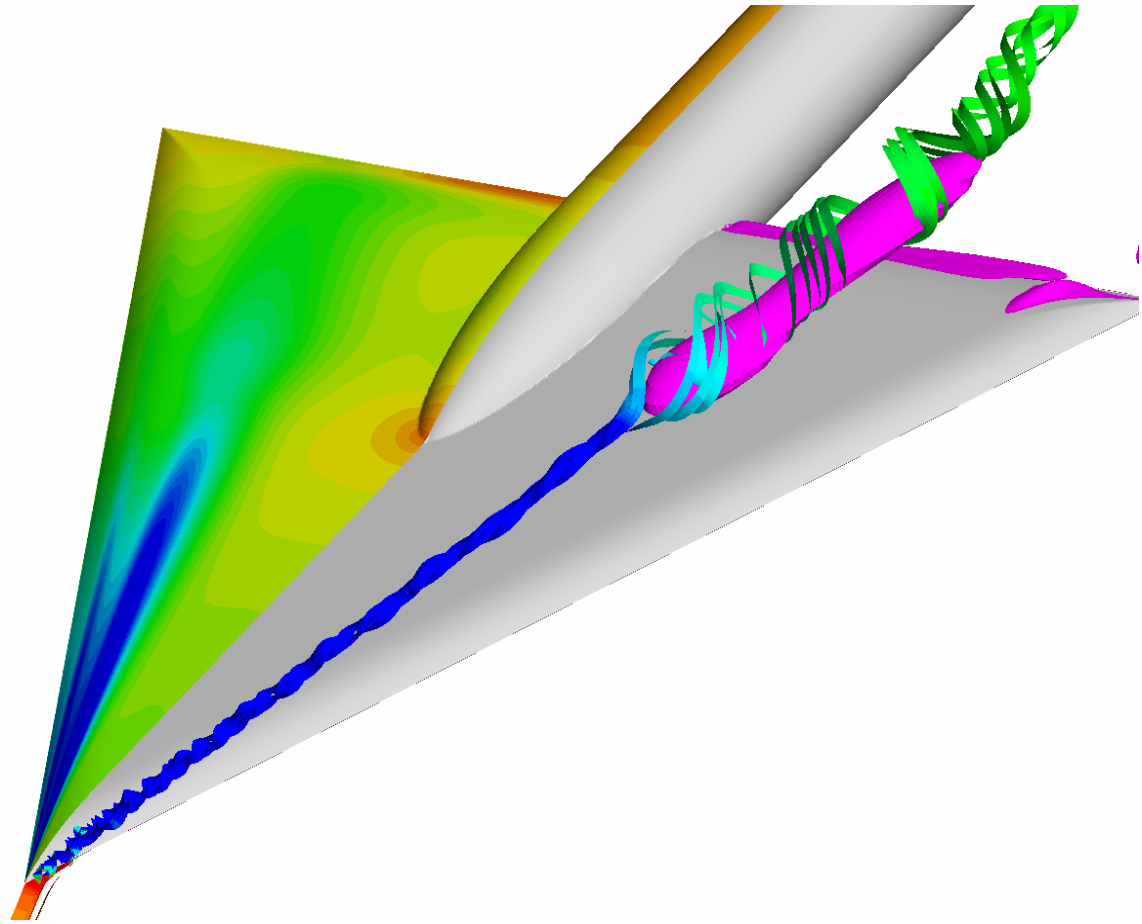

**Figure 34-19: Flow Features for Case 24: SLE, M = 0.40, α = 23°, Re = 6 x $10^6$.**

The comparison of the surface pressure contours for this test case is presented in Figure 34-20. Compared to the last test case (Figure 34-17), the structure is very similar, but the rapid decay of the leeward suction peak now begins farther upstream. This decay of the suction peak is due to the above mentioned widening of the vortex core and indicates the beginning of vortex breakdown in the numerical solutions. The onset point of this vortex breakdown is at about $x/c_r = 0.6$ in all numerical solutions. The EADS and KTH solutions are very similar and show a rather quick decay of the suction peak along the rear part of the wing, whereas the NLR solution shows a slower decay of this suction peak. In the experimental pressure distributions at $x/c_r = 0.6$ there is still a compact vortex present and the onset of vortex breakdown is somewhere near $x/c_r = 0.8$ (at the last cross section, the experimental pressure distribution shows clearly vortex breakdown; at $x/c_r = 0.8$ there is still a recognizable vortical flow structure, but the suction peak is less compact as in the upstream sections).

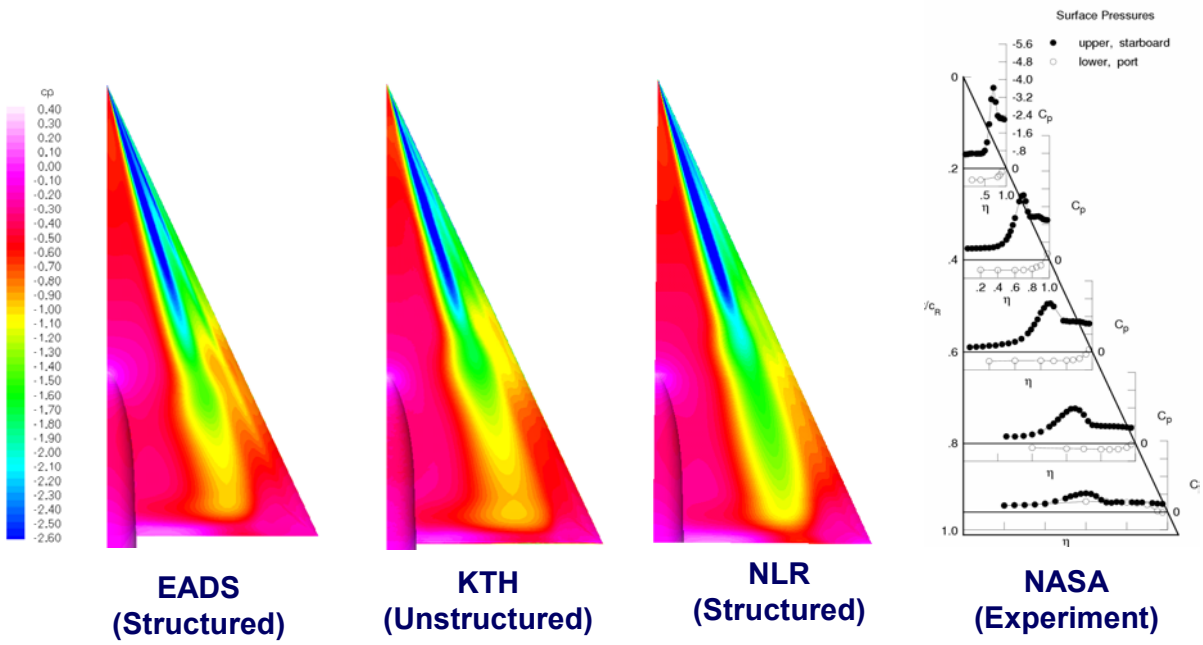


**Figure 34-20: Surface Pressure Maps for Case 24: SLE, M = 0.40, α = 23°, Re = 6 x $10^6$.**

The differences between experimental and numerical data can be seen in more details in the pressure comparisons shown in Figure 34-21. In the two most upstream cross sections the numerical solutions match the main flow features (effects of primary and secondary vortices) quite well. The differences are again in the levels of the main suction peak and in the details in the region of the secondary vortex. From $x/c_r = 0.6$ the agreement with the experimental pressure distribution is less good. All numerical solutions show a less compact and smeared out vortex compared to the experimental data. This may be related to the above mentioned widening of the vortex core, which may lead to a more upstream onset of vortex breakdown in the numerical calculations.

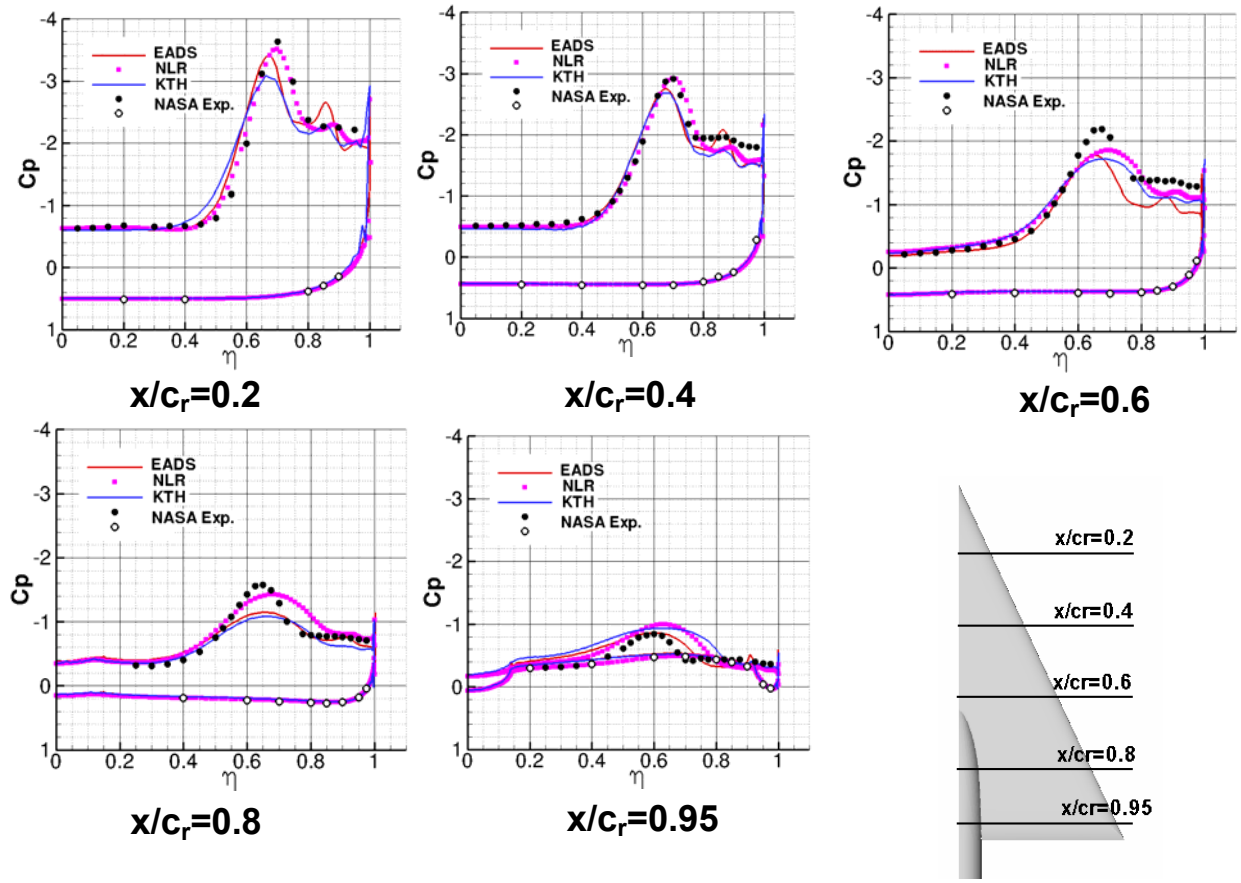


**Figure 34-21: Comparison of Surface Pressures and Experimental Data (Ref. [34-9]) for Case 24: SLE, M = 0.40, α = 23°, Re = 6 x $10^6$.**

### 34.6.6 Case 27: SLE, M = 0.85, α = 23°, Re = 6 x $10^6$

The last test case finally is a transonic one at high incidence. In the subsonic region (M = 0.4) it was seen in the experiments that vortex breakdown begins at about α = 21° at the rear end of the wing, and then continuously moves upstream with increasing angle of attack. In the transonic region however, the onset of vortex breakdown took place suddenly somewhere in the middle of the wing. The reason found for this sudden onset of breakdown is a shock/vortex interaction, which is triggering the breakdown. An impression of the surface shock structure and the 3-D vortical structure is given in Figure 34-22 (a detailed discussion of this test case is given in Ref. [34-14]).

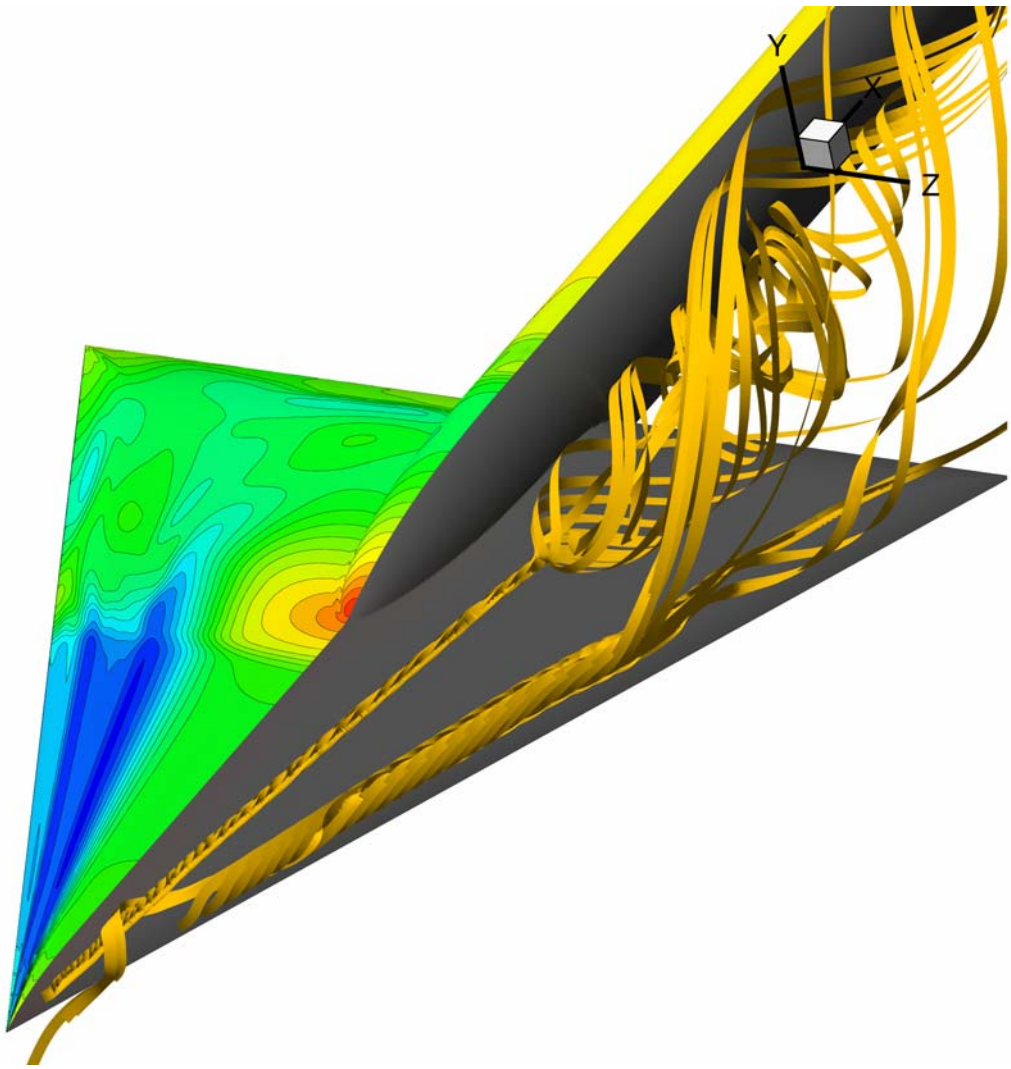


**Figure 34-22: Flow Features for Case 25: SLE, M = 0.85, α = 23°, Re = 6 x $10^6$.**

Figure 34-22 shows the surface pressure contours (left hand side) and 3-D volume ribbons along the core of the primary and secondary vortex (right hand side). The surface pressure contours show a very clear vortex structure on the forward part of the wing, consisting of a primary and a secondary vortex. At $x/c_r \approx 0.5$ there is a shock. Downstream of the shock the vortical flow structure vanishes very rapidly and a more dead water type pressure distribution develops. The visualization of the core of the primary vortex indicates a very compact vortex core upstream of the shock. Even across the shock this vortex core remains very compact. However, a very short distance downstream of the shock a sudden, very strong breakdown of the primary vortex occurs. The secondary vortex also seems to have vortex breakdown, but exactly at the shock position.

Figure 34-23 shows the surface pressure contours of four different numerical solutions together with the experimental data [34-9]. There are three very similar solutions (EADS, KTH, NLR) which all show the above mentioned vortex structure, the shock which is followed by vortex breakdown, and finally the dead water type flow over the rear part of the wing. However, the TAI solution looks completely different. The suction peak is

more smeared out and there is no significant effect of a secondary vortex. There is only a very weak shock, which is farther downstream, and the vortical structure is maintained downstream of the shock. This solution is more similar to the experimental data, which also indicates a vortical flow structure over the rear end of the wing.

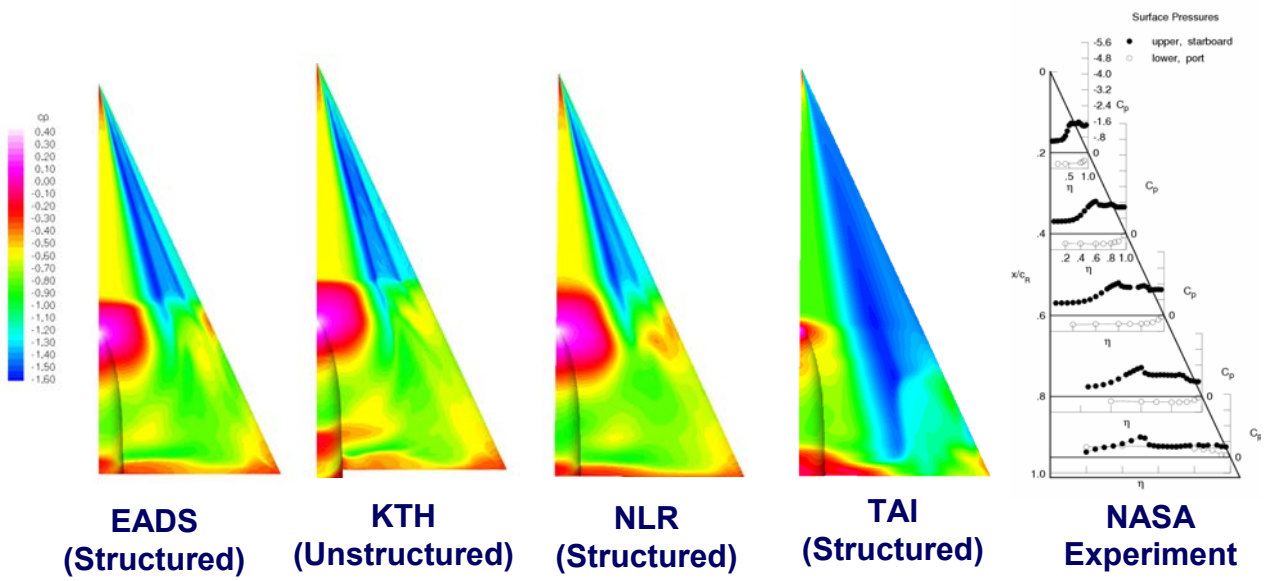


**Figure 34-23: Surface Pressure Maps for Case 25: SLE, M = 0.85, α = 23°, Re = 6 x $10^6$.**

The surface pressure distributions in Figure 34-24 underline the differences between the two classes of solutions. Upstream of the shock (at $x/c_r = 0.2$ and $x/c_r = 0.4$) the numerical results of EADS, NLR, and KTH are identical and match the experimental data. The TAI solution shows a lower suction peak, a much smoother inboard pressure gradient, and no significant effect of a secondary vortex. This indicates weaker vortices in the TAI solution compared to the experiment and to the other solutions.

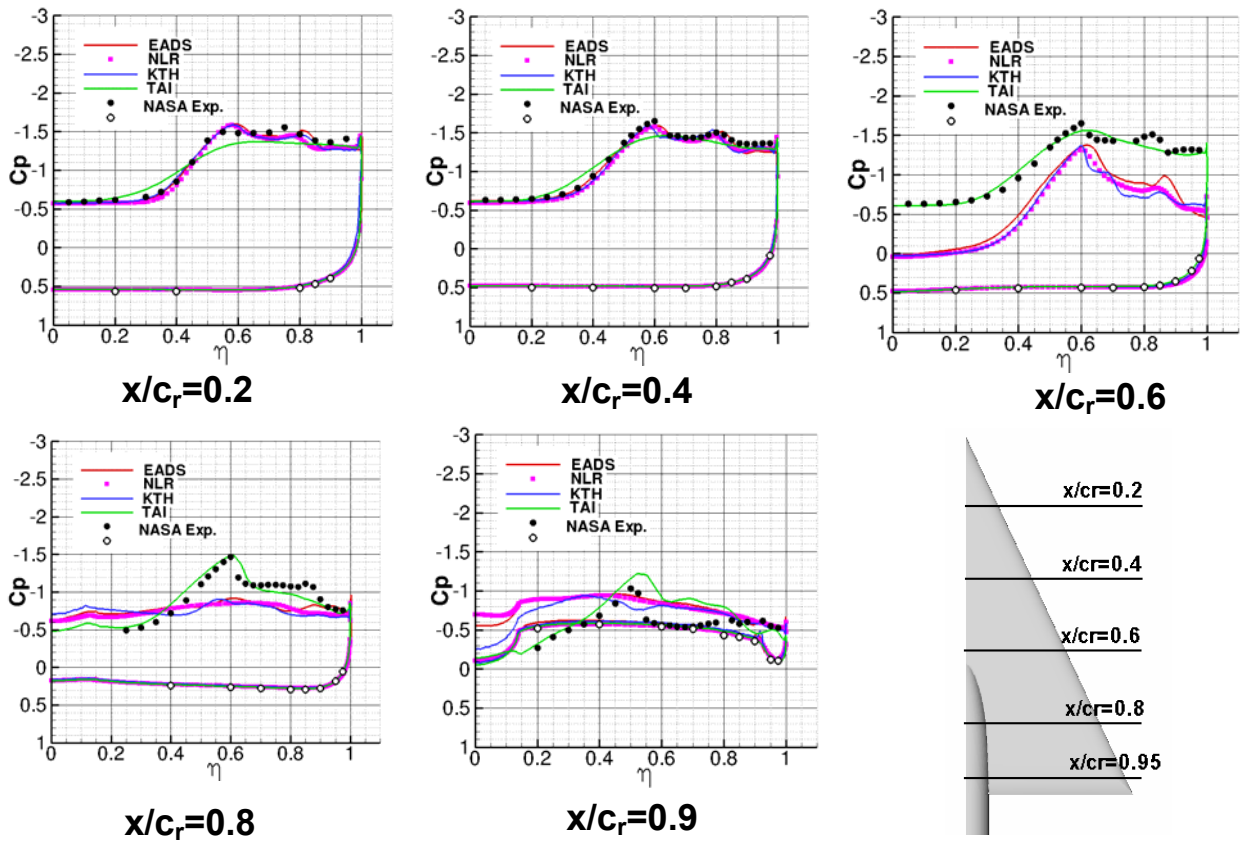


**Figure 34-24: Comparison of Surface Pressures and Experimental Data (Ref. [34-9]) for Case 25: SLE, M = 0.85, α = 23°, Re = 6 x $10^6$.**

At $x/c_r = 0.6$ the TAI solution does not yet show the effect of a shock, as is also shown in the experiment. Because of the weaker upstream shock, the agreement of the TAI solution at the inboard part of the wing is better than the other solutions. The suction peaks of primary and secondary vortex are however under-predicted. The other three solutions are again very similar and they all show the pressure jump due to the shock at $x/c_r \approx 0.5$. Because of these reasons the solutions do not match the experimental data, but they still show a vortical structure. In the cross sections $x/c_r = 0.8$ and $x/c_r = 0.95$ the solutions of EADS, NLR, and KTH all show a dead water type pressure distribution without any vortical structure, whereas the TAI solution fits the experimental data very well.

The main problem of this test case is the position of the shock. In the EADS, NLR, and KTH solutions the shock is too far upstream and too strong compared to the experiment. Because of this the vortical flow field downstream of the shock is destroyed and the experimental data cannot be matched. In Ref. [34-14], where this test case is discussed very intensively, it was seen that the problem of the forward upstream shock position is not affected by grid resolution or by different turbulence models. Even time-averaged DES simulations have shown the same problem. It was however also seen that this test case is very sensitive to small changes in the angle of incidence, as it is shown in Figure 34-25.

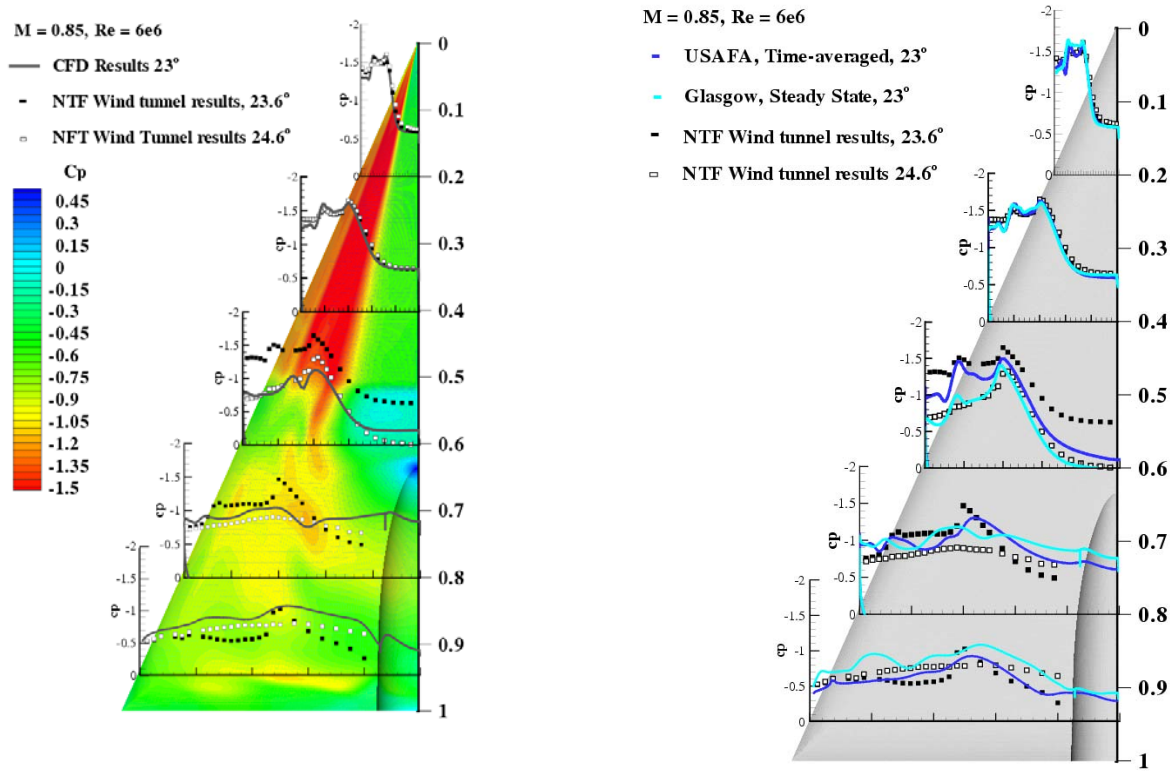


**Figure 34-25: Comparison of Surface Pressures and Experimental Data (Ref. [34-9]) for Case 25: SLE, M = 0.85, α = 23°, Re = 6 x $10^6$.**

Figure 34-25 shows on the left hand side the result of the University of Glasgow (UG) using a structured grid. It shows the same pattern as the three above mentioned solutions: an upstream position of the shock and dead water type flow downstream of the shock. The right hand side of Figure 34-25 shows the UG results together with the time-averaged DES results of USAFA. Also presented are experimental results [34-9] for α = 23.6° and α = 24.6°. This comparison shows that even the time-averaged DES results show the upstream shock with its consequences on breakdown. It also shows that if the experimental data from a higher angle of attack are taken for comparison, the agreement with the numerical data is very good and thus demonstrates the high sensitivity of the shock position to small changes in the angle of attack.

Figure 34-26 shows a detailed comparison between the EADS surface pressure contours (representative for the other numerical solutions), the surface pressure contours of the TAI solution and the experimental pressure distribution. The pressure gradients now appear more clearly. In the EADS solution there is a strong shock at $x/c_r \approx 0.5$, the dead water type of flow downstream of the shock, and a terminating shock at the inner part of the wing. It also shows a very significant secondary vortex which also interacts with the shock. The TAI solution shows a much weaker and more smeared out single vortex in the forward part of the wing. This weaker and less compact vortex obviously induces a weaker and more upstream positioned shock. The suction peak is only slightly reduced across this shock. More downstream, at $x/c_r \approx 0.8$, a second weak shock wave builds up from the wing leading edge towards the suction peak. When reaching the suction peak, this shock wave makes a 90° angle and becomes a weak cross flow shock, which finally merges with the terminating shock close to the trailing edge. This shock formation can also be concluded from the experimental pressure distribution. There is a

considerable pressure increase at the outer part of the wing between the last two wing sections. This indicates this second weak shock. The experimental pressure distributions at $x/c_r = 0.8$ and $x/c_r = 0.95$ also give an indication of a weak cross flow shock. This analysis indicates that in the five "common" solutions the axial velocities upstream of the shock are possibly too high and thus a too strong shock at a too much upstream position builds up. One reason therefore may be that a too strong (primary or secondary) vortex induces too high axial velocities in these numerical solutions.

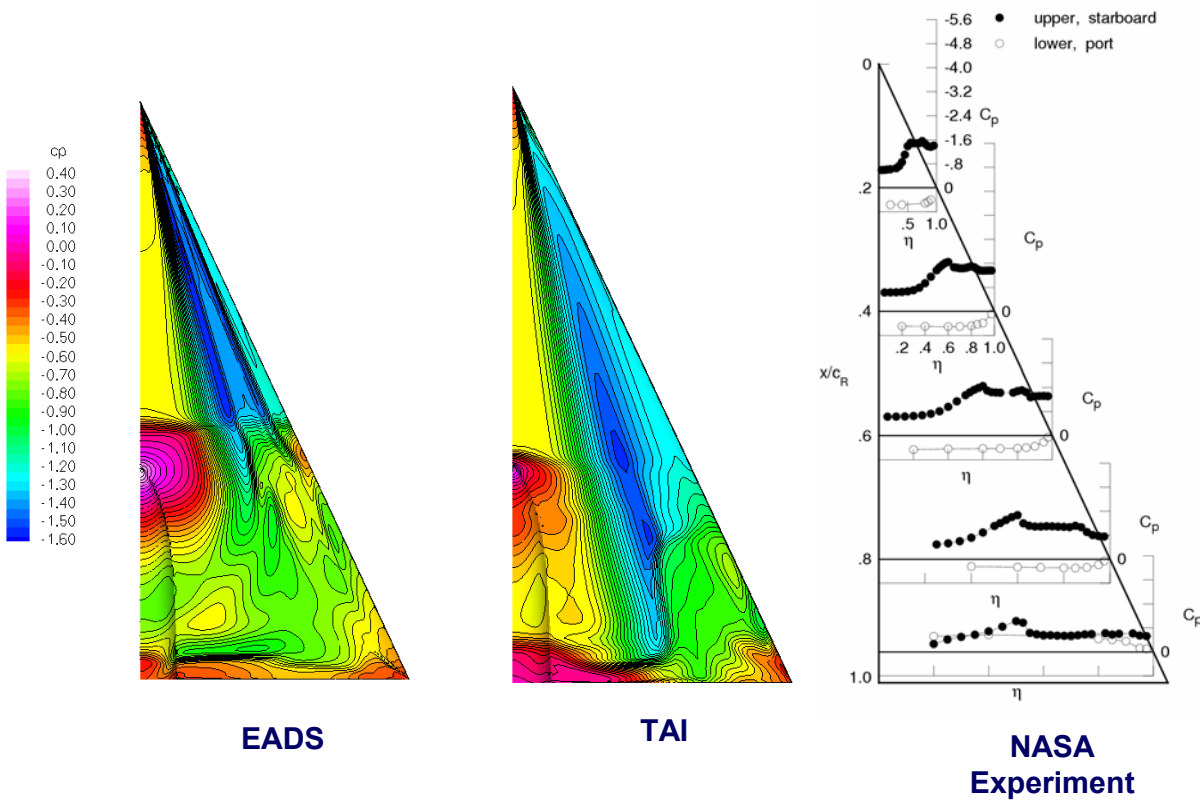


**Figure 34-26: Surface Pressure Maps for Case 25: SLE, M = 0.85, α = 23°, Re = 6 x $10^6$.**

Figure 34-27 finally shows a comparison of the skin friction magnitude of four different solutions. There are again the three "common" solutions (EADS, NLR, and KTH) and the TAI solution. The three "common" solutions show very clearly the effect of a primary and a secondary vortex. It is remarkable that the maximum skin friction at the secondary vortex has nearly the same magnitude as that of the primary vortex. This confirms the strong rotation of the secondary vortex, which could already be observed in the surface pressure contours (see Figure 34-23). The TAI solution shows no effect of a secondary vortex and also the primary vortex is less compact compared with the other solutions. This may be an additional indication that too compact vortices upstream of the shock may be the reason for a shock that is too strong and too much upstream in the other solutions.

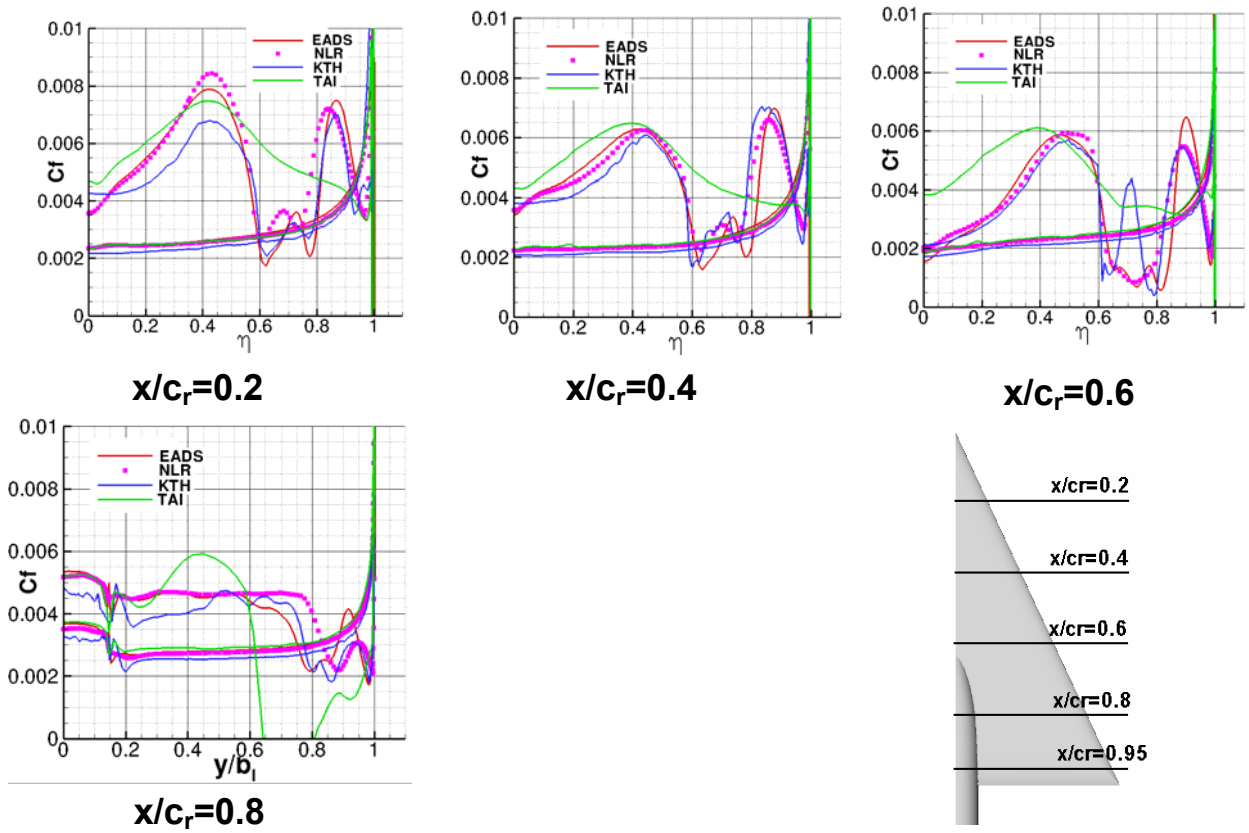


**Figure 34-27: Comparison of Skin Friction Predictions for Case 25: SLE, M = 0.85, α = 23°, Re = 6 x $10^6$.**

## 34.7 CONCLUSIONS AND RECOMMENDATIONS

From the comparisons of the different solutions for the different test cases the following conclusions and recommendations are drawn and given:

- The subsonic SLE test cases show the best agreement between the different numerical results and between numerical results and experiment. But even for these test cases with clearly defined leading edge separation the correct prediction of vortex break down is still a very difficult task. In all the numerical simulations presented here, vortex break down occurred at earlier angles of attack compared to the experiment. This may be due to an under-prediction of the axial velocity in the vortex core. Either there is still a deficit of the existing turbulence models for a proper treatment of vortical flow, or RANS methods are overstrained and DES methods are required for the correct prediction of vortex break down.
- In the transonic region there is the tendency that the shock position is predicted too much upstream and by this vortex break down is also predicted earlier as in the experiment. On the other hand vortex break down due to shock/vortex interaction is very sensitive to small changes in the angle of attack, which rises the question about the accuracy of the experimental data in such cases (is there an uncertainty or error band about the nominal angle of attack).
- For the test cases with round leading edge, the prediction of the onset of the primary leading edge is the most essential problem. The position of this separation point can be predicted too much upstream

or too much downstream or (by accident?) at the correct position. Depending on this, the agreement between numerical and experimental results can be very good or less good. One uncertainty parameter which was found for these test cases is the unknown transition, which can have a strong effect on the solution. So transition modeling should be further promoted. Another difficulty is the effect of the Reynolds number at delta wings with round leading edges. This effect also can be under- or over-predicted.

Summarizing it can be stated, that not for all test cases the experimental surface pressure distributions could be matched satisfactorily, but anyhow detailed numerical flow analysis gave an essential insight into some complex flow structures (double vortex system at round LE, shock vortex interaction in transonic flow) and the numerical calculations helped to design the PIV experiments.

## 34.8 ACKNOWLEDGEMENTS

The guidance and encouragement of Prof. Dietrich Hummel was instrumental in the completion of this work, for which the authors are grateful. The authors also would like to thank the other computational experimental researchers within the VFE-2 group who provided numerical solutions as well as experimental data for this paper.

## 34.9 REFERENCES

[34-1] Drougge, G.: *The International Vortex Flow Experiment for Computer Code Validation*, ICAS Proceedings, 1988, Vol. 1, pp. 35-41.

[34-2] Elsenaar, A., Hjelmberg, L., Bütefisch, K.-A. and Bannink, W.J.: *The International Vortex Flow Experiment*, AGARD-CP-437, Vol. 1, 1988, pp. 9-1 to 9-23.

[34-3] Wagner, B., Hitzel, S., Schmatz, M.A., Schwarz, W., Hilgenstock, A. and Scherr, S.: *Status of CFD Validation on the Vortex Flow Experiment*, AGARD-CP-437, Vol. 1, 1988, pp. 10-1 to 10-10.

[34-4] Hoeijmakers, H.W.M.: *Modelling and Numerical Simulation of Vortex Flow in Aerodynamics*, AGARD-CP-494, 1991, pp. 1-1 to 1-46.

[34-5] Ekaterinaris, J.A. and Schiff, L.B.: *Numerical Simulation of Incidence and Sweep Effects on Delta Wing Vortex Breakdown*, Journal of Aircraft, Vol. 31, No. 5, 1994, pp. 1043-1049.

[34-6] Mitchell, A.M., Morton, S.A., Forsythe, J.R. and Cummings, R.M.: *Analysis of Delta-Wing Vortical Substructures Using Detached-Eddy Simulation*, AIAA Journal, Vol. 44, No. 5, 2006, pp. 964-972.

[34-7] Hummel, D. and Redeker, G.: *A New Vortex Flow Experiment for Computer Code Validation*, RTO AVT Symposium on "Vortex Flow and High Angle of Attack Aerodynamics", Loen Norway, RTO-MP-069, 2003, pp. 8-1 to 8-31.

[34-8] Hummel, D.: *The Second International Vortex Flow Experiment (VFE-2): Objective and First Results*, 2nd International Symposium on "Integrating CFD and Experiments in Aerodynamics", Cranfield University, 2005.

[34-9] Chu, J. and Luckring, J.M.: *Experimental Surface Pressure Data Obtained on 65° Delta Wing Across Reynolds Number and Mach Number Ranges*, NASA TM 4645, 1996.

[34-10] Londenberg, W.K.: *Transonic Navier-Stokes Calculations about a 65 Degree Delta Wing*, NASA-CR-4635, November 1994.

[34-11] Chiba, K. and Obayashi, S.: *CFD Visualization of Second Primary Vortex Structure on a 65-Degree Delta Wing*, AIAA Paper 2004-1231, January 2004.

[34-12] Fritz, W.: *Numerical Simulation of the Peculiar Subsonic Flow-Field about the VFE-2 Delta-Wing with Rounded Leading-Edge*, AIAA Paper 2008-0393, January 2008.

[34-13] Gürdamar, E.: *Influence of Grid Resolution on the Accuracy of High Angle of Attack Delta Wing Simulations*, AIAA Paper 2008-0394, January 2008.

[34-14] Schiavetta, L., Boelens, O.J., Crippa, S., Cummings, R.M., Fritz, W. and Badcock, K.J.: *Shock Effects on Delta Wing Vortex Breakdown*, AIAA Paper 2008-0395, January 2008.

[34-15] Cummings, R.M. and Schütte, A.: *Detached-Eddy Simulation of the Vortical Flowfield about the VFE-2 Delta Wing*, AIAA Paper 2008-0396, January 2008.

[34-16] Crippa, S.: *Steady, Subsonic CFD Analysis of the VFE-2 Configuration and Comparison to Wind Tunnel Data*, AIAA Paper 2008-0397, January 2008.

[34-17] Schütte, A. and Lüdeke, H.: *Numerical Investigations on the VFE-2 Rounded Leading Edge Configuration using the Unstructured DLR TAU Code*, AIAA Paper 2008-0398, January 2008.

[34-18] Luckring, J.: *What was Learned from the New VFE-2 Experiments*, AIAA Paper 2008-0383, January 2008.

[34-19] Konrath, R., Schröder, A. and Kompenhans, J.: *Analysis of PIV Results Obtained for the VFE-2 65° Delta Wing Configuration at Sub- and Transonic Speeds*, AIAA Paper 2006-3003, June 2006.

# Appendix 34-1

This is a full listing of the cases considered for the VFE-2 numerical simulation project. The cases in bold were considered to be important for the subsonic analysis, while Cases 18 and 27 were important to the transonic analysis.

**Table 34-A1: Full List of the Cases Considered within VFE-2 Numerical Simulations**

| Case No. | Old Case No. | $\alpha$ (deg.) | Leading Edge | $M_\infty$ | $Re_{\bar{c}}$ (millions) |
|---|---|---|---|---|---|
| 1 | None | 13.3 | RLE | 0.2 | 1 |
| 2 | None | 13.3 | RLE | 0.2 | 2 |
| 3 | None | 13.3 | SLE | 0.2 | 2 |
| **4** | **12** | **13.3** | **RLE** | **0.4** | **2** |
| **4.5** | **None** | **13.3** | **RLE** | **0.4** | **3** |
| **5** | **11** | **13.3** | **RLE** | **0.4** | **6** |
| **6** | **9** | **13.3** | **SLE** | **0.4** | **6** |
| 7 | None | 13.3 | RLE | 0.85 | 2 |
| 8 | None | 13.3 | RLE | 0.85 | 6 |
| 9 | None | 13.3 | SLE | 0.85 | 6 |
| 10 | None | 18.5 | RLE | 0.2 | 1 |
| 11 | None | 18.5 | RLE | 0.2 | 2 |
| 12 | None | 18.5 | SLE | 0.2 | 2 |
| **13** | **6** | **18.5** | **RLE** | **0.4** | **2** |
| **14** | **5** | **18.5** | **RLE** | **0.4** | **6** |
| **15** | **1** | **18.5** | **SLE** | **0.4** | **6** |
| 16 | 8 | 18.5 | RLE | 0.85 | 2 |
| 17 | 7 | 18.5 | RLE | 0.85 | 6 |
| 18 | 3 | 18.5 | SLE | 0.85 | 6 |
| 19 | None | 23.0 | RLE | 0.2 | 1 |
| 20 | None | 23.0 | RLE | 0.2 | 2 |
| 21 | None | 23.0 | SLE | 0.2 | 2 |
| **22** | **18** | **23.0** | **RLE** | **0.4** | **2** |
| **23** | **17** | **23.0** | **RLE** | **0.4** | **6** |
| **24** | **13** | **23.0** | **SLE** | **0.4** | **6** |
| 25 | 20 | 23.0 | RLE | 0.85 | 2 |
| 26 | 19 | 23.0 | RLE | 0.85 | 6 |
| 27 | 15 | 23.0 | SLE | 0.85 | 6 |